



# Facile fabrication of BUC-21/Bi<sub>24</sub>O<sub>31</sub>Br<sub>10</sub> composites for enhanced photocatalytic Cr(VI) reduction under white light

Chen Zhao<sup>a,b</sup>, Zhihua Wang<sup>a,\*</sup>, Xiang Li<sup>b</sup>, Xiaohong Yi<sup>b</sup>, Hongyu Chu<sup>b</sup>, Xi Chen<sup>b</sup>, Chong-Chen Wang<sup>b,\*</sup>

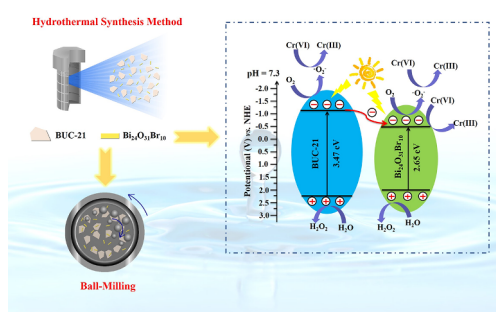
<sup>a</sup> State Key Laboratory of Chemical Resource Engineering, Beijing University of Chemical Technology, Beijing 100029, China

<sup>b</sup> Beijing Key Laboratory of Functional Materials for Building Structure and Environment Remediation/Beijing Advanced Innovation Centre for Future Urban Design, Beijing University of Civil Engineering and Architecture, Beijing 100044, China

## HIGHLIGHTS

- It is the first report on hydrothermal synthesis of Bi<sub>24</sub>O<sub>31</sub>Br<sub>10</sub> nanosheets.
- BUC-21/Bi<sub>24</sub>O<sub>31</sub>Br<sub>10</sub> (BB-x) composites were prepared by a simple ball-milling method.
- BB-x composites exhibited superior activity toward Cr(VI) reduction.
- BB-x composites could act as stable white-light-responsive photocatalysts.

## GRAPHICAL ABSTRACT



## ARTICLE INFO

### Keywords:

Metal-organic framework  
Bi<sub>24</sub>O<sub>31</sub>Br<sub>10</sub> nanosheet  
Cr(VI) reduction  
White light  
Photocatalysis

## ABSTRACT

In this study, the Bi<sub>24</sub>O<sub>31</sub>Br<sub>10</sub> nanosheets were successfully synthesized using hydrothermal method. Subsequently, series binary BUC-21/Bi<sub>24</sub>O<sub>31</sub>Br<sub>10</sub> composites were fabricated by facile ball-milling method. The results suggested that the introduction of a specific quality of Bi<sub>24</sub>O<sub>31</sub>Br<sub>10</sub> on the surface of BUC-21 could enhance the utilization efficiency of white light and suppress the photo-induced carriers recombination to promote the photocatalytic efficiency. The BB-100 (the mass ratio of BUC-21/Bi<sub>24</sub>O<sub>31</sub>Br<sub>10</sub> being 1) exhibited the best performance, in which 99.9% Cr(VI) ions were photoreduced into Cr(III) upon the white light irradiation within 120 min. As well, the influences of small organic acids, initial pH, light intensities along with the co-existing matters on the Cr(VI) removal were investigated. Furthermore, the Box-Behnken experimental design methodology proved that the photoreduction process was significantly influenced by the co-existing inorganic anions and negatively charged dissolved organic matters (DOM). After 4-run recycling for the adsorption-photoreduction of Cr(VI) experiments, the BB-100 still exhibited satisfied reduction activity with good stability and reusability. A possible reaction mechanism was proposed and clarified through the electrochemical determination, time-resolved photoluminescence decay spectra, active species trapping experiments, electron spin resonance analyses (ESR) and density functional theory (DFT) calculation.

\* Corresponding authors.

E-mail addresses: [zhwang@mail.buct.edu.cn](mailto:zhwang@mail.buct.edu.cn) (Z. Wang), [wangchongchen@bucea.edu.cn](mailto:wangchongchen@bucea.edu.cn) (C.-C. Wang).

<https://doi.org/10.1016/j.cej.2019.123431>

Received 7 July 2019; Received in revised form 31 October 2019; Accepted 7 November 2019

Available online 09 November 2019

1385-8947/ © 2019 Elsevier B.V. All rights reserved.

## 1. Introduction

Hexavalent chromium (Cr(VI)) is an extremely harmful pollutant in various aquatic environments, which was originated from several industrial activities including but not limited to printing, pigments, leather tanning, electroplating [1–4]. Being compared with low-toxic and stable form of trivalent chromium Cr(III), Cr(VI) might exert enormous threat to human being and the other organisms due to its ultra-high toxicity, mutagenicity, carcinogenicity and high solubility [5–8]. Therefore, the transformation from Cr(VI) to Cr(III) is imperative for the sake of reducing toxicity and weakening mobility of Cr(VI). Up to now, a range of techniques including chemical reduction [9–12], electron-reduction [11,13,14], micro-reduction [15,16] and photocatalytic reduction [2,17] have been used to achieve Cr(VI) reduction in industrial effluent. Nevertheless, among the reduction methods, the photocatalytic Cr(VI) reduction under UV, visible, UV/visible or even solar light is deemed as an effective, green and low-cost way for eliminating Cr(VI) pollution, which attracted considerable attentions in field of environment remediation [2,18–20].

Metal-organic frameworks (MOFs) have been developed rapidly in environmental photocatalysis in recent decades [2,19,21–23]. Their predominant photocatalytic activity can be ascribed to the abundant catalytically active sites (metal-ligand nodes), functional organic linkers, metal-oxo clusters, specific surface area, tunable pore size, designable framework architecture as well as the possibility to be functionalized [22,24–26]. For example, Zn-containing MOFs ZIF-8 had been proven to have sufficient removal efficiency and recyclability for oxidation of methylene blue [27]. Zr-based MOFs NH<sub>2</sub>-UiO-66 could be excited under visible light and exhibited outstanding activities toward photodegrading organic contaminants and photoreduction of Cr(VI) [28–30]. Amino-modified Ti(IV)-based MOFs NH<sub>2</sub>-MIL-125 acted as a preeminent photocatalyst to accomplish transform from amines to imines [31] and Cr(VI) photoreduction under visible light illumination [32]. Morsali's research group has synthesized TMU-series MOFs-based photocatalysts, which exhibited good photocatalytic activity in photo-oxidative desulfurization (PODS) process and organic pollution removal [33–35]. BUC-21 is a newly synthesized Zn-based 2D MOFs, which exhibited superior activity for Cr(VI) removal under UV light illumination [36,37]. Nevertheless, band gap energy ( $E_g$ ) of BUC-21 is approximately 3.4 eV [36], implying its low solar energy utilization efficiency. Additionally, the photocatalytic application of pristine MOFs is inefficient due to their poor electronic conductivity [22,38–40]. Therefore, the combination of MOFs with other light-harvesting and highly conductive inorganic semiconductors might be an effective strategy [41–45].

Bismuth-based photocatalysts have attracted increasing attentions because of their non-toxicity, significant availability and chemical inertness [46–49]. As a narrow band gap semiconductor (approximately 2.7 eV), Bi<sub>24</sub>O<sub>31</sub>Br<sub>10</sub> is a competitive candidate for harvesting the solar energy [50]. Up to now, it has been applied for Cr(VI) photoreduction [50], H<sub>2</sub> generation [50] and organic contaminants degradation [51–54]. However, as a fast-growing photocatalyst, Bi<sub>24</sub>O<sub>31</sub>Br<sub>10</sub> still has two inherent drawbacks. Firstly, a green and simple synthesis method was urgently needed. For example, chemical precipitation combined with post-heating treatment (the samples calcined at 300–800 °C) was mainly used for the synthesis of Bi<sub>24</sub>O<sub>31</sub>Br<sub>10</sub> [50,55]. Alternatively, microwave-assisted reaction [51,53] and organic solvothermal process (ethylene glycol or glycerol was applied as the solvent) [52,54] were also carried out to synthesize Bi<sub>24</sub>O<sub>31</sub>Br<sub>10</sub> photocatalysts. Up to now, there is no literature about hydrothermal synthesis of Bi<sub>24</sub>O<sub>31</sub>Br<sub>10</sub>. Secondly, the rapid recombination of photo-generated electron-hole pairs significantly led to the declined photocatalytic performance [56]. To overcome the above shortcomings, fabrication of effective composite photocatalysts should be further studied. Recently, He et al. reported the construction of NiFe<sub>2</sub>O<sub>4</sub>/Bi<sub>24</sub>O<sub>31</sub>Br<sub>10</sub> by thermal decomposition method [57]. Liu and co-workers first synthesized Bi<sub>4</sub>O<sub>5</sub>Br<sub>2</sub>/

Bi<sub>24</sub>O<sub>31</sub>Br<sub>10</sub>/Bi<sub>2</sub>SiO<sub>5</sub> heterojunctions using in-situ ion exchange reaction [58]. All these composites displayed high-efficiency photocatalytic performances due to their synergistic effects. However, to the best of our knowledge, MOF/Bi<sub>24</sub>O<sub>31</sub>Br<sub>10</sub> composite photocatalysts haven't been developed so far.

In this study, Bi<sub>24</sub>O<sub>31</sub>Br<sub>10</sub> was firstly synthesized using hydrothermal method. Furthermore, Bi<sub>24</sub>O<sub>31</sub>Br<sub>10</sub> was successfully coupled with highly-efficient MOF photocatalyst (BUC-21) to generate the BUC-21/Bi<sub>24</sub>O<sub>31</sub>Br<sub>10</sub> composites by the facile ball-milling method. The optical properties, morphologies and structures of BUC-21/Bi<sub>24</sub>O<sub>31</sub>Br<sub>10</sub> (BB-x, x is the weight percentage of Bi<sub>24</sub>O<sub>31</sub>Br<sub>10</sub> according to the BUC-21) composites were characterized, and their photocatalytic activities toward Cr(VI) reduction were evaluated upon the illumination of the white light. The results revealed that as-prepared BB-100 could achieve highest photoreduction efficiency. The improved performance might be ascribed to the accelerated separation rate of electron-hole pairs and efficient utilization of white light. Furthermore, BB-100 exhibited good stability and recyclability after 4-run recycling experiments. The plausible reaction mechanism for the Cr(VI) removal over BUC-21/Bi<sub>24</sub>O<sub>31</sub>Br<sub>10</sub> was also proposed and tested.

## 2. Experimental

### 2.1. Fabrication of photocatalysts

#### 2.1.1. Synthesis of BUC-21

BUC-21 was synthesized by the solvothermal method as reported in the previous literatures [36,37,59]. Briefly, a mixture of 0.0410 g ZnCl<sub>2</sub>, 0.0470 g 4,4'-bipyridine, 0.1070 g *cis*-1,3-dibenzyl-2-oxo-4,5-imidazolidinedicarboxylic acid and 18.0 mL H<sub>2</sub>O was sealed in a 25.0 mL Teflon-lined autoclave and heated at 160 °C for 3 d. Finally, through the processes of centrifugation, filtration, washing and drying, the white crystals of BUC-21 were obtained.

#### 2.1.2. Synthesis of Bi<sub>24</sub>O<sub>31</sub>Br<sub>10</sub>

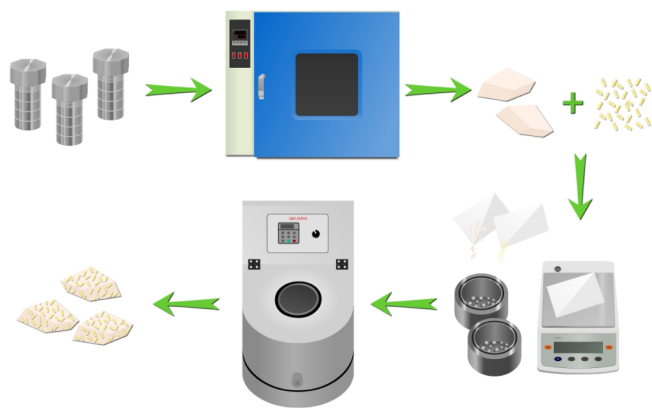
In this study, the nanosheets of Bi<sub>24</sub>O<sub>31</sub>Br<sub>10</sub> were directly synthesized by hydrothermal method. Specifically, 1.000 g Bi(NO<sub>3</sub>)<sub>3</sub>·5H<sub>2</sub>O and 1.000 g cetyltrimethyl ammonium bromide (C<sub>16</sub>H<sub>33</sub>(CH<sub>3</sub>)<sub>3</sub>NBr, CTAB) were dissolved in 40.0 mL ultrapure water with the aid of stirring 15 min. Then, the pH value of the solution was adjusted to 11.5 by adding 1 mol/L NaOH aqueous solution. The obtained suspension was stirred at room temperature for 45 min, and then transferred into 100 mL autoclave. After heating at 160 °C for 18 h, the resulting precipitates were washed with ultrapure water and ethanol in turn, finally dried at 80 °C under vacuum for 12 h.

#### 2.1.3. Fabrication of BUC-21/Bi<sub>24</sub>O<sub>31</sub>Br<sub>10</sub>

The BUC-21/Bi<sub>24</sub>O<sub>31</sub>Br<sub>10</sub> composites were prepared by ball-milling method (Scheme 1). Briefly, the mixed powders were ground in a Nanjing Nanda planet-type grinding mill system at 30 Hz for 20 min. The details of composites with different amount of BUC-21 and Bi<sub>24</sub>O<sub>31</sub>Br<sub>10</sub> were illustrated in Table 1. Furthermore, the as-prepared materials were characterized by XRD, FT-IR, UV-vis DRS, PL, XPS, SEM, TEM, HRTEM, ESR, electrochemical analysis, etc. The details about these characterization techniques, Box-Behnken methodology and DFT calculations were shown in Supporting Information (ESI).

### 2.2. Photocatalytic performance measurement

The photocatalytic activities of the as-prepared materials were evaluated through the photoreduction from Cr(VI) into Cr(III). About 50.0 mg of the materials were added to 200 mL Cr(VI) solution with the initial concentration being 10 mg/L, in which the initial pH values were adjusted with diluted H<sub>2</sub>SO<sub>4</sub> or NaOH. In order to achieve the adsorption-desorption equilibrium between photocatalysts and Cr(VI) solutions, the reaction suspension was continually stirred in



**Scheme 1.** The preparation procedure of BUC-21/Bi<sub>24</sub>O<sub>31</sub>Br<sub>10</sub> composites.

**Table 1**

The designations of the BUC-21/Bi<sub>24</sub>O<sub>31</sub>Br<sub>10</sub> composites with various dosages of Bi<sub>24</sub>O<sub>31</sub>Br<sub>10</sub>.

No.	BUC-21/mg	Bi <sub>24</sub> O <sub>31</sub> Br <sub>10</sub> /mg	Sample name
1	100	25	BB-25
2	100	50	BB-50
3	100	75	BB-75
4	100	100	BB-100
5	100	125	BB-125
6	100	150	BB-150

photophobic condition for 40 min prior to the photoreaction. Upon the white light irradiation provided by 500 W Xe light (the spectrum of the used light source was shown in Fig. S1), 2.0 mL the aqueous solution was extracted and filtered through 0.45  $\mu$ m membrane filter at certain time intervals for subsequent measurements. The concentration of residual Cr(VI) in the samples was colorimetrically measured at 540 nm using the diphenylcarbazide method in a Laspec Alpha-1860 UV-vis spectrophotometer [30,60].

### 2.3. Electrochemical test

The Mott-Schottky curves, electrochemical impedance spectroscopy (EIS) and the photocurrent analysis were measured on a Metrohm Autolab PGSTAT204 electrochemical workstation. A Pt electrode and a saturated Ag/AgCl electrode were applied as the reference electrode and the counter electrode, respectively. The as-prepared photocatalysts (BUC-21, Bi<sub>24</sub>O<sub>31</sub>Br<sub>10</sub> or BB-100) were fabricated on the FTO substrate to be the working electrodes following the procedure listed as below: 0.005 g samples were dispersed in 400  $\mu$ L of ethanol-Nafion (19/1 v/v) to generate homogeneous slurry with the help of sonication for 30 min, and the suspension was drop-casted on a FTO substrate (1 cm  $\times$  1 cm). All the tests were carried out in 0.2 mol/L Na<sub>2</sub>SO<sub>4</sub> solutions (pH = 7.3) at room temperature and a 300 W Xe lamp was applied as light source.

## 3. Results and discussions

### 3.1. Characterizations

The powder X-ray diffraction (PXRD) patterns of BUC-21, Bi<sub>24</sub>O<sub>31</sub>Br<sub>10</sub> and series composites were depicted in Fig. 1(a). The diffraction peaks of BUC-21 powder were perfectly in agreement with the PXRD patterns simulated from the single crystal data of BUC-21 [36,37], indicating that BUC-21 was successfully synthesized. The Bi<sub>24</sub>O<sub>31</sub>Br<sub>10</sub> sample displayed the strong diffraction peaks of (1 0 2), (2 0 6), (2 1 3), (1 1 7), (2 0 1) and (0 1 1) crystal planes at 10.5°, 25.1°, 29.8°, 31.8°, 46.0° and 57.0°, respectively. All diffraction peaks matched well with the standard XRD patterns (JCPDS No. 75-0888), indicating

that the monoclinic phase of Bi<sub>24</sub>O<sub>31</sub>Br<sub>10</sub> (A2/m) was fabricated in this work. As to the BUC-21/Bi<sub>24</sub>O<sub>31</sub>Br<sub>10</sub> composites, the PXRD patterns were consistent with both of BUC-21 and Bi<sub>24</sub>O<sub>31</sub>Br<sub>10</sub> structures, suggesting the co-existence of BUC-21 and Bi<sub>24</sub>O<sub>31</sub>Br<sub>10</sub> phases. In detail, the characteristic peaks at 13.6°, 15.9°, 20.5° and 25.5° were assigned to the pristine BUC-21, whereas the peaks at 10.5°, 29.8°, 31.8°, 46.0° and 57.0° could be attributed to the Bi<sub>24</sub>O<sub>31</sub>Br<sub>10</sub>.

The functional groups together with chemical bonding of materials can be detected by Fourier transform infrared (FT-IR) spectra. As illustrated in Fig. 1(b), the wide and strong peak in the range of 3250–3600 cm<sup>-1</sup> was probably assigned to the stretching vibrations of -OH of adsorbed water molecules [61,62]. In the FT-IR spectrum of BUC-21, the peaks at 1645 and 1417 cm<sup>-1</sup> were attributed to the asymmetric and symmetric vibrations of C = O, whereas C-N stretching vibrations were observed at 1220 and 1141 cm<sup>-1</sup> [36]. Being compared with the spectrum of BUC-21, the broad peak centered at 1621 cm<sup>-1</sup> was belong to the Bi-O stretching vibrations in Bi<sub>24</sub>O<sub>31</sub>Br<sub>10</sub> [57]. The well-matched FT-IR peaks of the series of composites further confirmed that Bi<sub>24</sub>O<sub>31</sub>Br<sub>10</sub> was interacted with BUC-21 successfully.

As shown in Fig. 1(c), the BUC-21 photocatalyst possessed absorption maxima at 248 and 320 nm, whereas Bi<sub>24</sub>O<sub>31</sub>Br<sub>10</sub> exhibited notable visible light absorption at wavelengths between 400 and 600 nm. Obviously, the absorption edge of the series of as-prepared materials was similar with that of pure Bi<sub>24</sub>O<sub>31</sub>Br<sub>10</sub> with long tails at the longer wavelengths, and the optical absorption intensity was decreased gradually in the visible region range with the increase of BUC-21 content. It was also implied that forming composites between the BUC-21 and Bi<sub>24</sub>O<sub>31</sub>Br<sub>10</sub> led to enhance absorption ability both in UV and visible light regions, which might be ascribed to the synergistic effect between both photocatalysts. Therefore, the aforementioned results revealed that the as-prepared materials might have photocatalytic activity under UV-visible light [63,64].

The  $E_g$  of BUC-21, Bi<sub>24</sub>O<sub>31</sub>Br<sub>10</sub> and the corresponding composites were calculated through the Tauc's plots, as illustrated in Fig. 1(d). The  $E_g$  values of BUC-21 and Bi<sub>24</sub>O<sub>31</sub>Br<sub>10</sub> were about 3.47 and 2.65 eV, respectively, which were close to those reported in the literatures [36,50,51]. It is notable that the  $E_g$  of the corresponding composites tended to turn narrower after the addition of Bi<sub>24</sub>O<sub>31</sub>Br<sub>10</sub>, and the composites demonstrated light yellow color, which was quite different from the white color of BUC-21. Those phenomena suggested that the response of the as-prepared photocatalysts under the visible light could be obviously enhanced, thus might improve the photoreduction performance by generating more photo-generated electron-hole pairs [2,22].

The scanning electron microscopy (SEM), transmission electron microscopy (TEM) and high-resolution transmission electron microscopy (HRTEM) images of BUC-21, Bi<sub>24</sub>O<sub>31</sub>Br<sub>10</sub> and BB-100 were illustrated in Fig. 2. As exhibited in Fig. 2(a) and (d), BUC-21 displayed the polyhedron structures, which were consistent with the observation reported previously [37]. As to Bi<sub>24</sub>O<sub>31</sub>Br<sub>10</sub> (Fig. 2(b) and (e)), it possessed irregular nanosheets and smooth surface with 100–500 nm in width. Moreover, BB-100 was chosen to be the representative sample for further investigations. From Fig. 2(e) and (f), it can be found that the surface of BB-100 was relatively rough, which could be attributed to that Bi<sub>24</sub>O<sub>31</sub>Br<sub>10</sub> nanosheets were distributed uniformly and highly dispersed on the surface of BUC-21. Fig. 2(g) and (h) further confirmed that the composites were successfully formed between Bi<sub>24</sub>O<sub>31</sub>Br<sub>10</sub> (bright parts) and BUC-21 (dark parts). In Fig. 2(f), Bi<sub>24</sub>O<sub>31</sub>Br<sub>10</sub> in composites revealed the fringe spacings of 0.841 and 0.251 nm, which can be indexed to the (1 0 -2) and (-3 0 8) crystal planes in Bi<sub>24</sub>O<sub>31</sub>Br<sub>10</sub> (JCPDS No. 75-0888). Moreover, the EDS elemental mappings (Fig. 3) suggested that the targeted elements (Zn, Bi, Br, N and O) were uniformly distributed over BB-100.

X-ray photoelectron spectroscopy (XPS) analysis was carried out for the purpose of exploring the elemental binding states of the fabricated composites (Fig. 4). As illustrated in Fig. 4(a), the XPS survey spectrum

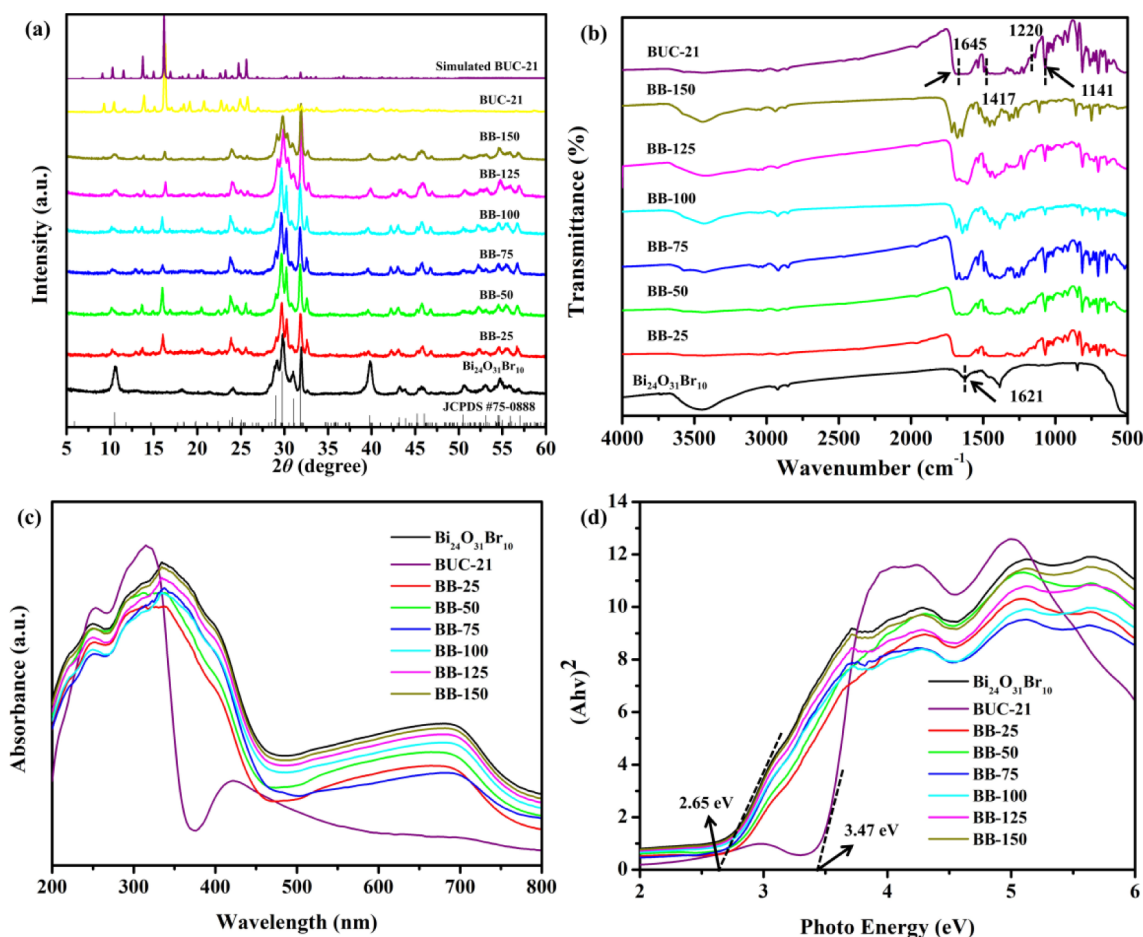


Fig. 1. (a) PXRD patterns, (b) FT-IR spectra, (c) UV-vis DRS and (d)  $E_g$  plots of BUC-21, Bi<sub>24</sub>O<sub>31</sub>Br<sub>10</sub>, and the corresponding BUC-21/Bi<sub>24</sub>O<sub>31</sub>Br<sub>10</sub> nanocomposites.

displayed that the dominating elements of BB-100 were C, N, O, Zn, Bi and Br. The C 1s spectrum obtained at high resolution was shown in Fig. 4(b), which can be curve-fitted into four different peaks at 284.5, 284.8, 285.7 and 288.6 eV. The peaks at 284.5 and 285.7 eV can be assigned to C=C/C-C and C-O present in the *cis*-1,3-dibenzyl-2-oxo-4,5-imidazolidinedicarboxylic acid, respectively [65,66], and the peaks at 284.8 and 288.6 eV can be attributed to C-H and N-C=O of BUC-21 [67]. The N 1s spectrum in Fig. 4(c) displayed two peaks at 399.1 and 400.0 eV, corresponding to the N-H and sp<sup>2</sup> hybridized N atoms in C=N of bpy [68,69]. Fig. 4(d) displayed the high resolution O 1s spectrum, in which the two peaks at 529.6 and 531.8 eV can be assigned to the Bi-O bonds of BB-100 and O-H groups of BUC-21, respectively [70]. From Fig. 4(e), the two peaks at 1022.4 and 1045.5 eV in the Zn 2p spectrum can be assigned to Zn 2p<sub>3/2</sub> and Zn 2p<sub>1/2</sub>, respectively. A comparison of Bi 4f XPS spectra of Bi<sub>24</sub>O<sub>31</sub>Br<sub>10</sub> and BB-100 was present in Fig. 4(f). It can be observed that the two peaks at 164.5 and 159.2 eV were ascribed to Bi 4f<sub>7/2</sub> and Bi 4f<sub>5/2</sub> in pristine Bi<sub>24</sub>O<sub>31</sub>Br<sub>10</sub>, respectively [71,72]. For BB-100 composite, the Bi 4f spectrum can be split up two peaks at about 163.8 and 158.5 eV, respectively, which were lower than that of Bi<sub>24</sub>O<sub>31</sub>Br<sub>10</sub>. For Br 3d spectrum, the characteristic peak at 68.3 eV was indexed to Br<sup>-</sup> in BB-100 (Fig. 4(g)) [73]. Furthermore, the remarkable shift (-0.4 eV) to lower binding energy in Br 3d spectrum of BB-100 was also observed. Energy shifts found in both Bi 4f and Br 3d spectra might be ascribed to the change of chemical environment caused by the interaction between Bi<sub>24</sub>O<sub>31</sub>Br<sub>10</sub> and BUC-21. It is well known that the binding energy of the target element is affected by its electron density [74,75]. The electron-rich BUC-21 may transfer some electrons to Bi<sub>24</sub>O<sub>31</sub>Br<sub>10</sub>, resulting in the increased electron density of Bi<sub>24</sub>O<sub>31</sub>Br<sub>10</sub>. Therefore, the Bi 4f and Br 3d peaks of BB-100 composite were shifted

to the lower binding energies [74,75]. Additionally, the nitrogen adsorption-desorption experiments revealed that the BET surface areas of the as-prepared materials increased to a certain extent (as shown in Table S1), from 1.10 m<sup>2</sup>/g (BUC-21) to 5.36 m<sup>2</sup>/g (BB-150), further indicating the BUC-21/Bi<sub>24</sub>O<sub>31</sub>Br<sub>10</sub> composites had been successfully synthesized.

### 3.2. Photocatalytic performance for removal of Cr(VI)

The feasibility of photocatalytic decontamination of Cr(VI) by BUC-21, Bi<sub>24</sub>O<sub>31</sub>Br<sub>10</sub>, BB-25, BB-50, BB-75, BB-100, BB-125 and BB-150 was investigated under white light, as illustrated in Fig. 5. In order to make clear the nature of reaction, control experiment was firstly conducted. The results revealed that the reduction of Cr(VI) was negligible in the dark or in the absence of photocatalyst. Moreover, all the composites showed better photocatalytic performance than those of pure BUC-21 (22.2%) and Bi<sub>24</sub>O<sub>31</sub>Br<sub>10</sub> (36.5%). As shown in Fig. 5(a), the photocatalytic activities of BUC-21/Bi<sub>24</sub>O<sub>31</sub>Br<sub>10</sub> composites were strongly related to the additive amount of Bi<sub>24</sub>O<sub>31</sub>Br<sub>10</sub> in the composite. When Bi<sub>24</sub>O<sub>31</sub>Br<sub>10</sub> was introduced into BUC-21, the removal efficiency was increased from 48.7% achieved by BUC-21 to 99.9% over BB-100 composite. Additionally, the pseudo-first-order kinetic model was applied to calculate the photoreduction rate over different photocatalysts [2]. It can be observed that photocatalytic activity of BB-100 displayed the fastest reduction rate ( $0.06287 \pm 0.00314 \text{ min}^{-1}$ ), which was 30.7 and 16.7 times higher than those of pure BUC-21 ( $0.00205 \pm 0.00006 \text{ min}^{-1}$ ) and Bi<sub>24</sub>O<sub>31</sub>Br<sub>10</sub> ( $0.00377 \pm 0.00007 \text{ min}^{-1}$ ), respectively (Fig. 5(b)). The improvement of the photocatalytic activities could be ascribed to the broadening of the light absorption spectrum,



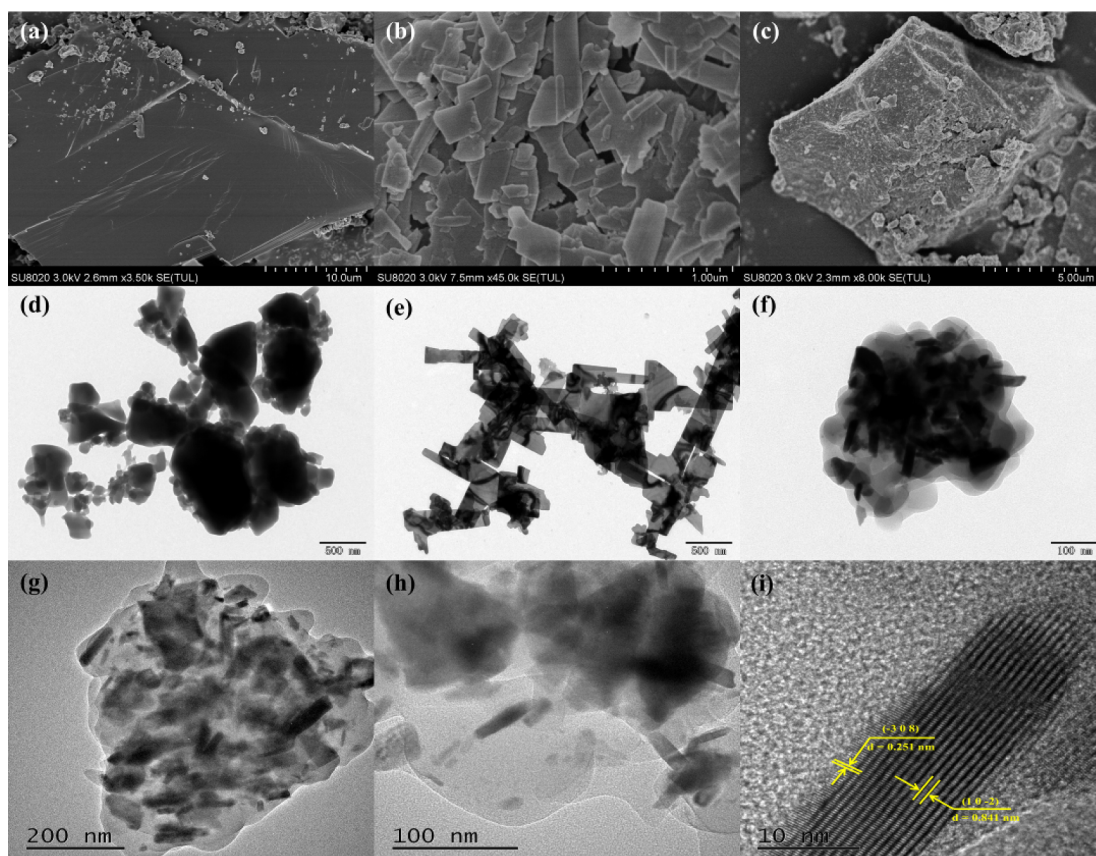


Fig. 2. SEM and TEM images of (a, d) BUC-21, (b, e)  $\text{Bi}_{24}\text{O}_{31}\text{Br}_{10}$ , (e, f) BB-100 and (g-i) HRTEM images of BB-100.

along with the suppressed recombination of electron-hole pairs in BUC-21 with the addition of  $\text{Bi}_{24}\text{O}_{31}\text{Br}_{10}$  in the composites. However, when the amount of  $\text{Bi}_{24}\text{O}_{31}\text{Br}_{10}$  was further increased beyond the optimal proportion like BB-100 (volcanic peak) [76], the photocatalytic activity was inclined to deteriorate, which was similar to the previous studies [37,60,77]. Additionally, the photocatalytic performance of Cr(VI) removal between BB-100 and the other photocatalysts reported in recent years was also compared as shown in Table 2. The results revealed that BB-100 was a white light-responsive photocatalyst with excellent performance for Cr(VI) reduction.

### 3.2.1. Effect of various hole scavengers

The effect of hole scavengers on the photoreduction of Cr(VI) was explored in the presence of three small molecular weight organic acids (SOAs), namely oxalic acid, citric acid and tartaric acid. As exhibited in Fig. 6, the photoreduction rate of Cr(VI) was enhanced by the introduction of above-mentioned SOAs, which followed the order of no SOAs ( $0.06287 \pm 0.00314 \text{ min}^{-1}$ ) < oxalic acid ( $0.06737 \pm 0.00623 \text{ min}^{-1}$ ) < citric acid ( $0.07348 \pm 0.00355 \text{ min}^{-1}$ ) < tartaric acid ( $0.08169 \pm 0.00656 \text{ min}^{-1}$ ). This result suggested that the photoreduction of Cr(VI) under white light irradiation over BB-100 was strongly related to the chemical structure of organic compounds, which

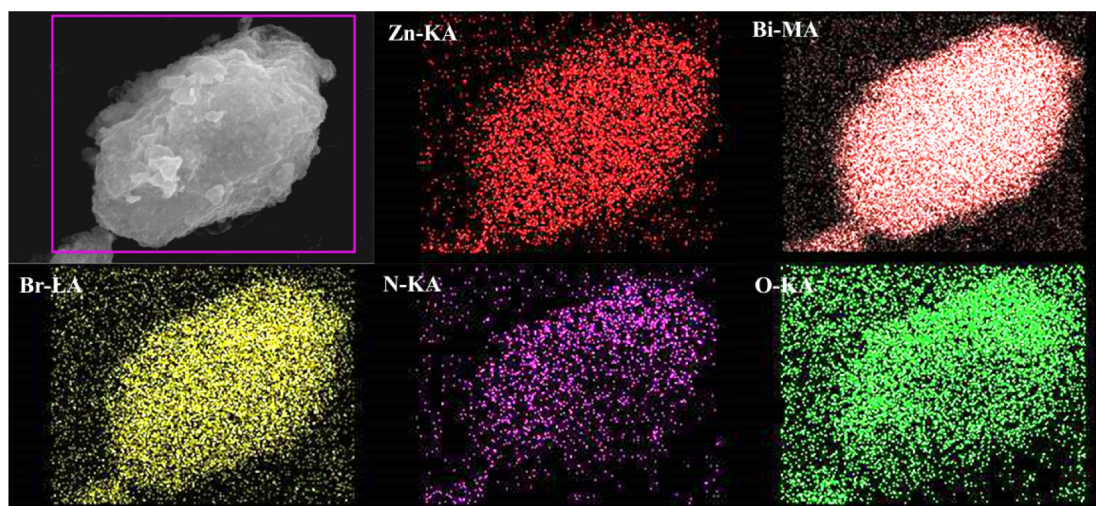


Fig. 3. The EDS elemental mappings of BB-100 composite.

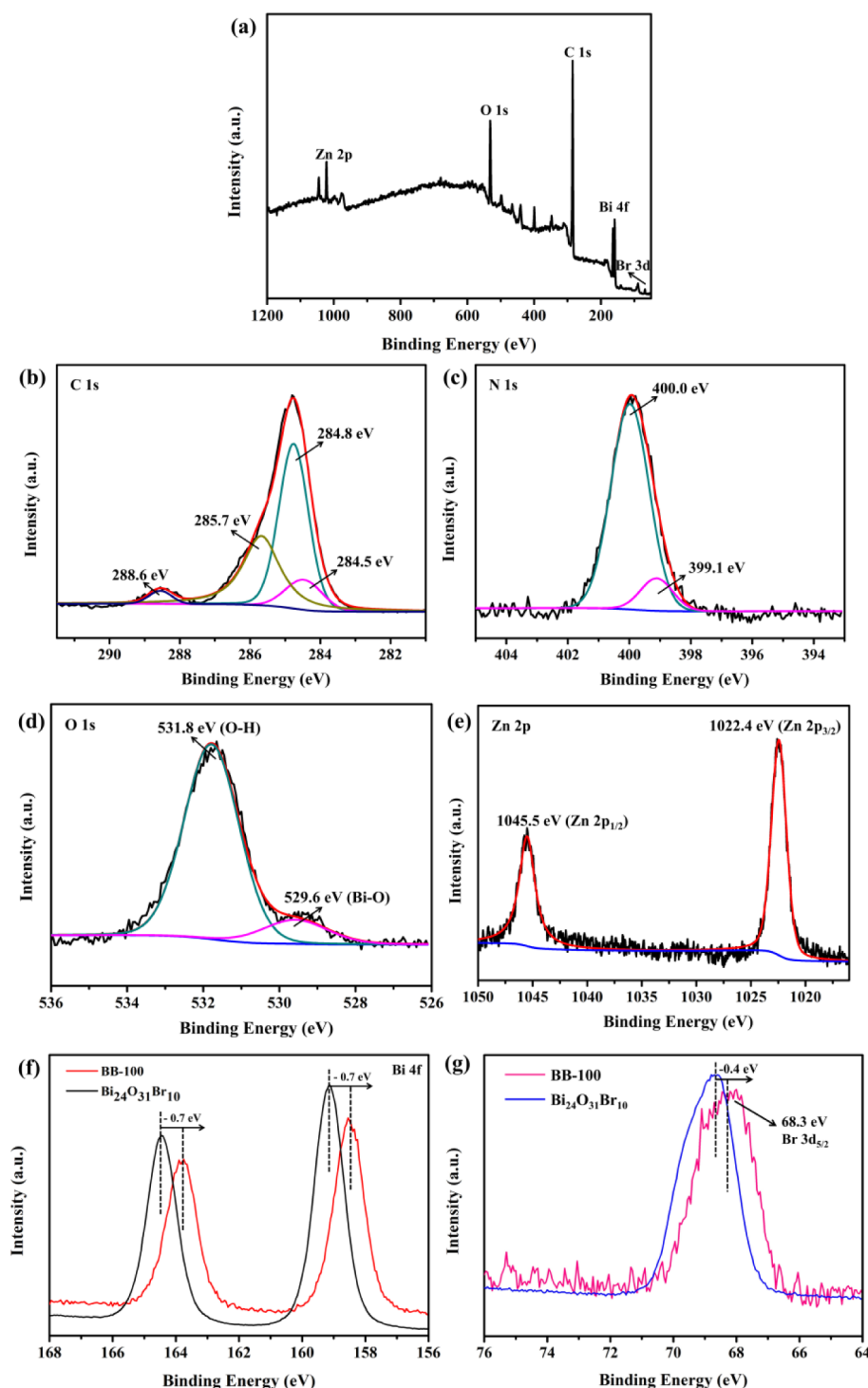


Fig. 4. XPS spectra of BB-100: (a) survey, (b) C 1s, (c) N 1s, (d) O 1s, (e) Zn 2p; the comparisons of (f) Bi 4f and (g) Br 3d spectra.

was similar to the former reports that the presence of different SOAs could change the photoreduction rates of Cr(VI) [87,88]. Actually, photooxidation of the sacrificial organic acids can markedly influence the coupled photoreduction rate of Cr(VI) by photo-generated electrons. The added SOAs might be oxidized by photo-generated holes or attacked by generated  $\cdot\text{OH}$  radicals. The SOAs have different abilities of trapping reactive oxygen species, resulting in the chemical structure dependence of the photoreduction performance for Cr(VI) removal under light irradiation [2]. Furthermore, the other excitation pathway of photo-generated electron had been explained by a well-known charge-transfer-complex theoretical model between the SOAs and metal

site on the surface of photocatalysts [89,90]. Therefore, the white light irradiation induced the intramolecular electron transfer from SOAs to BB-100, resulting in the generation of organic radicals ( $\text{RCO}_2^{\cdot-}$ ), which can also reduce Cr(VI) into Cr(III) [87,91].

### 3.2.2. Effect of initial pH of the reaction solution

Investigation on the solution pH is significant in the adsorption-photoreduction process since it might influence the existing form of Cr(VI) ions and the surface potential of the photocatalyst [19,86]. The concentration changes of residual Cr(VI) over BB-100 at various pH values were illustrated in Fig. 7. Evidently, the photoreduction

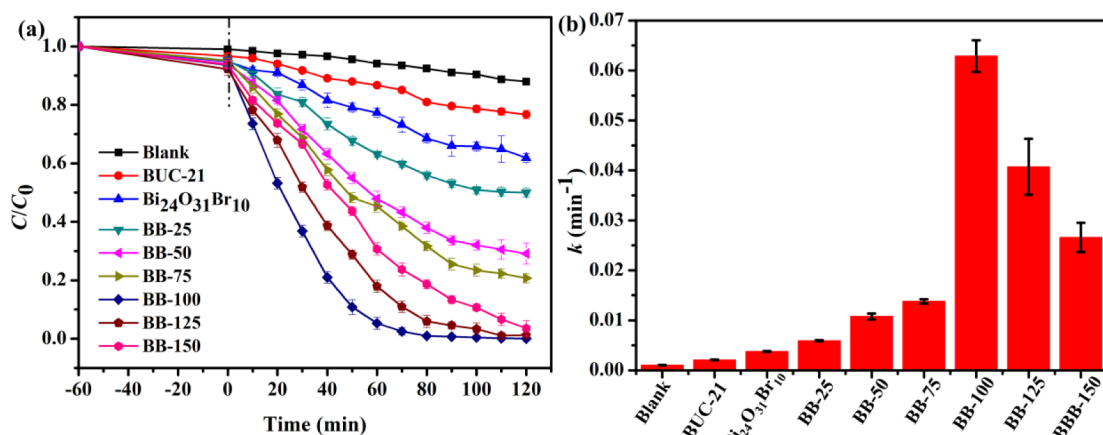


**Fig. 5.** (a) Photoreduction of the Cr(VI) at pH = 2 using various photocatalysts after 120 min white light irradiation and (b) their corresponding apparent reaction rate constants ( $k$ ).

**Table 2**

Comparative performance of typical photocatalysts for Cr(VI) reduction.

Photocatalysts	Experimental conditions						Reduction efficiency (%)	Reference
	pH	Dose (mg)	Volume (mL)	Concentration (mg/L)	Time (min)	Light source		
MIL-68(In)-NH <sub>2</sub>	2.0	40	40	20	180	300 W Xe lamp (> 420 nm)	97	[78]
Pd@UiO-66(NH <sub>2</sub> )	2.0	20	40	10	90	300 W Xe lamp (> 420 nm)	100	[29]
RGO-UiO-66(NH <sub>2</sub> )	2.0	20	40	10	100	500 W Xe lamp (> 420 nm)	100	[79]
CuS@MIL-125	2.1	25	50	48	70	500 W Xe lamp (> 420 nm)	52	[2]
g-C <sub>3</sub> N <sub>4</sub> @MIL-53(Fe)	2.0	20	50	10	180	500 W Xe lamp (> 420 nm)	99	[77]
WO <sub>3</sub> @MIL-53(Fe)	2.5	20	100	45	240	Sunlight	94	[80]
Bi <sub>2</sub> S <sub>3</sub> nanosphere	2.0	20	40	40	120	500 W Xe lamp (> 420 nm)	90	[81]
Bi <sub>2</sub> WO <sub>6</sub> nanosheet	–	60	50	10	120	300 W Xe lamp (> 420 nm)	100	[82]
g-BN@BiOCl	2.0	32	40	10	150	300 W Xe lamp (> 420 nm)	92	[83]
p-NiO@n-Nb <sub>2</sub> O <sub>5</sub>	2.0	50	50	58	300	500 W Tungsten lamp	100	[84]
Cu <sub>2</sub> O@BiVO <sub>4</sub>	–	50	100	9	120	300 W Xe lamp (> 420 nm)	100	[85]
g-C <sub>3</sub> N <sub>4</sub> @GO@BiFeO <sub>3</sub>	2.0	500	200	5	120	300 W Xe lamp (> 400 nm)	100	[86]
BB-100	2.0	50	200	10	120	500 W Xe lamp	99	This work

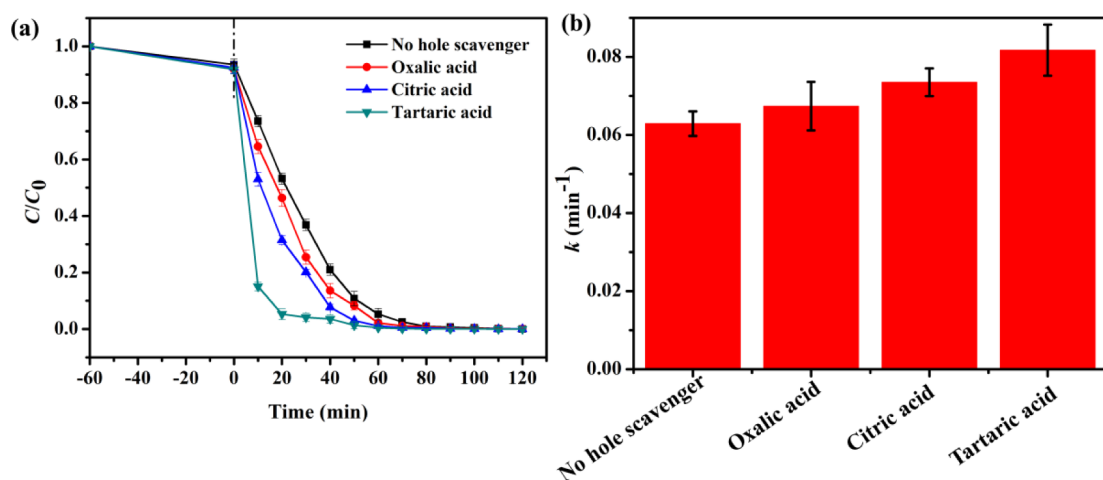
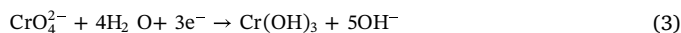
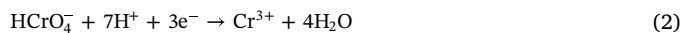
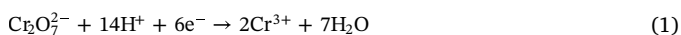


**Fig. 6.** (a) Photoreduction of Cr(VI) with different SOAs and (b) their corresponding  $k$  values. Conditions: BB-100 = 50 mg, Cr(VI) = 10 mg/L, 200 mL, pH = 2.0.

efficiency can be increased rapidly by the decreasing pH values (99.9%, 76.3%, 37.1%, 15.3%, 9.6% at pH = 2, 3, 4, 6 and 8, respectively). Under different pH circumstances, Cr(VI) ions present in different forms [2,19]. When  $2 < \text{pH} < 6$ , the dominating form of Cr(VI) is  $\text{Cr}_2\text{O}_7^{2-}$  or  $\text{HCrO}_4^-$ , and the photocatalytic reduction of Cr(VI) occurs following the Eqs. (1) and (2). Under the alkaline surroundings,  $\text{CrO}_4^{2-}$  is the main specie, leading to a reaction as expressed in Eq. (3).



It is obvious that the acidic medium is favorable for photoreduction of Cr(VI) because of the presence of substantial  $\text{H}^+$ . It was noteworthy to noting that BB-100 displayed the greatest adsorption capacity at pH = 2 (4.5%), which can be ascribed to that the zeta potential of BB-100 became more negative with the increase of pH values (as illustrated



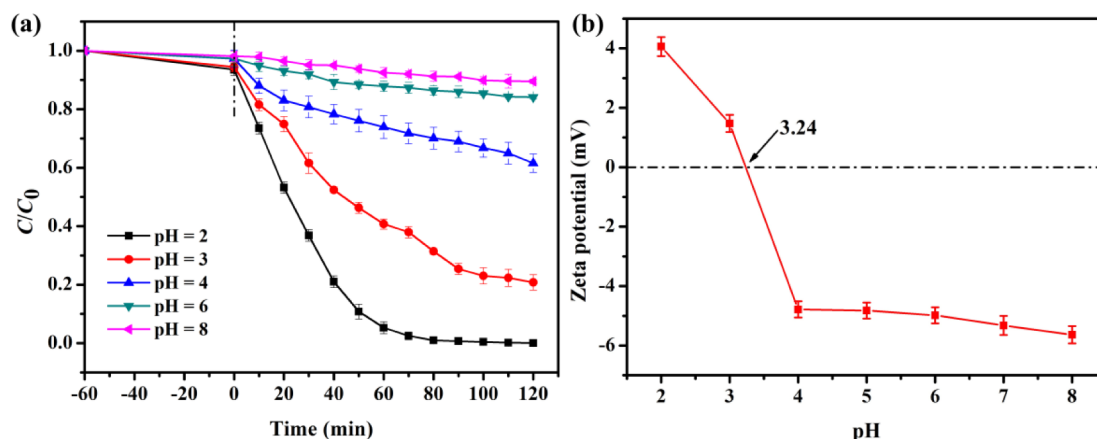


Fig. 7. (a) Effect of initial pH values on Cr(VI) reduction, (b) Zeta potential of BB-100 as a function of pH value.

in Fig. 7(b)). The isoelectric point of BB-100 was determined to be ca. 3.24, hence the zeta potential of the BB-100 was positive when the  $\text{pH} < 3.24$ . The surface of the BB-100 had stronger adsorption activity toward anionic Cr(VI), thereby the Cr(VI) ions can be continuously accumulated on the surface of BB-100 to enhance the ability of capturing photo-generated electrons and ultimately improved the photoreduction efficiency of Cr(VI) under acidic conditions. However, the surface charge of the BB-100 became negative at higher pH conditions, which tended to adsorb the cationic Cr(III) and electrostatically repel the anionic Cr(VI) [78]. The interfacial resistance made it difficult for the anionic Cr(VI) to gain the photo-generated electrons. Moreover, when  $\text{pH} > 6$ , the  $\text{Cr}(\text{OH})_3$  precipitates were inclined to be formed on the surface of BB-100, which could cover the active sites of photocatalysts, thereby decreasing its photocatalytic performance [17].

### 3.2.3. Effect of light intensity

For general photocatalytic reaction, with the increase of light intensity, the number of photons absorbed by the photocatalyst will also increase, thus enhancing the corresponding photocatalytic efficiency. The effect of light intensity on pseudo-first-order kinetic constant of Cr(VI) photoreduction was investigated at  $\text{pH} = 2.0$ . As shown in Fig. 8(a), the Cr(VI) removal efficiencies decreased with the lower light intensity (40.7%, 76.7% and 99.9% corresponded to 15.18, 24.25 and 46.07  $\text{mW}/\text{cm}^2$ , respectively). The  $k$  values were consistent with the photoreduction efficiencies, following the order of 15.18  $\text{mW}/\text{cm}^2$  ( $0.00492 \pm 0.00027 \text{ min}^{-1}$ ) < 24.25  $\text{mW}/\text{cm}^2$  ( $0.01381 \pm 0.00092 \text{ min}^{-1}$ ) < 46.07  $\text{mW}/\text{cm}^2$  ( $0.06287 \pm 0.00314 \text{ min}^{-1}$ ). Therefore, the  $k$  values were found to increase almost linearly with light intensity with the presence of 0.5 g/L BB-100 particles in reaction

solution (Fig. 8(b)), which was similar to the typical semiconductor photocatalyst reported previously [92].

### 3.2.4. Effect of co-existing matters

The presence of co-existing ions and dissolved organic matter (DOM) might affect the Cr(VI) adsorption-photoreduction behaviors during photocatalytic process. In order to investigate the practical applications of as-prepared photocatalysts, real lake water and tap water were selected to prepare Cr(VI) solutions to proceed photocatalytic reaction under the optimal experimental condition. The water quality parameters of the above two types of waters were shown in Table S2. As shown in Fig. 9(a), the photoreduction percentages of Cr(VI) were decreased significantly in lake water (72.0%) and tap water solutions (62.2%). And the  $k$  values followed the order of tap water ( $0.00635 \pm 0.00015 \text{ min}^{-1}$ ) < lake water ( $0.01071 \pm 0.00021 \text{ min}^{-1}$ ) < ultrapure water ( $0.06287 \pm 0.00314 \text{ min}^{-1}$ ) (Fig. 9(b)). As the surface of BB-100 was positively charged at  $\text{pH} = 2$ , which facilitated the adsorption of inorganic anions ( $\text{Cl}^-$ ,  $\text{NO}_3^-$ ,  $\text{SO}_4^{2-}$  and  $\text{PO}_4^{3-}$ ) and negatively charged DOM on the active sites of the BB-100 through electrostatic attraction. Hence there was a competition in adsorption between the co-existing anions and  $\text{Cr}_2\text{O}_7^{2-}$ , thus weakening the photoreduction efficiency [37,93]. Meanwhile, it can be observed that the photoreduction rate of Cr(VI) was decreased in tap water compared to that in lake water, which might be mainly ascribed to the different concentrations of the co-existing organic components. As illustrated in Fig. 9(c) and (d), excitation-emission matrix (EEM) spectra indicated that fluorescence signals of the lake and tap water samples located at  $E_x/E_m = 230\text{--}245/380\text{--}400 \text{ nm}$ , which were

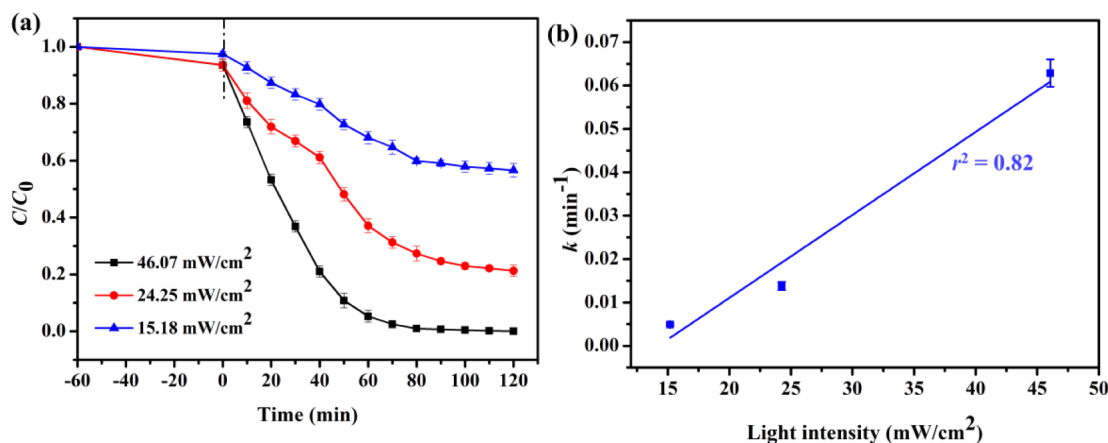
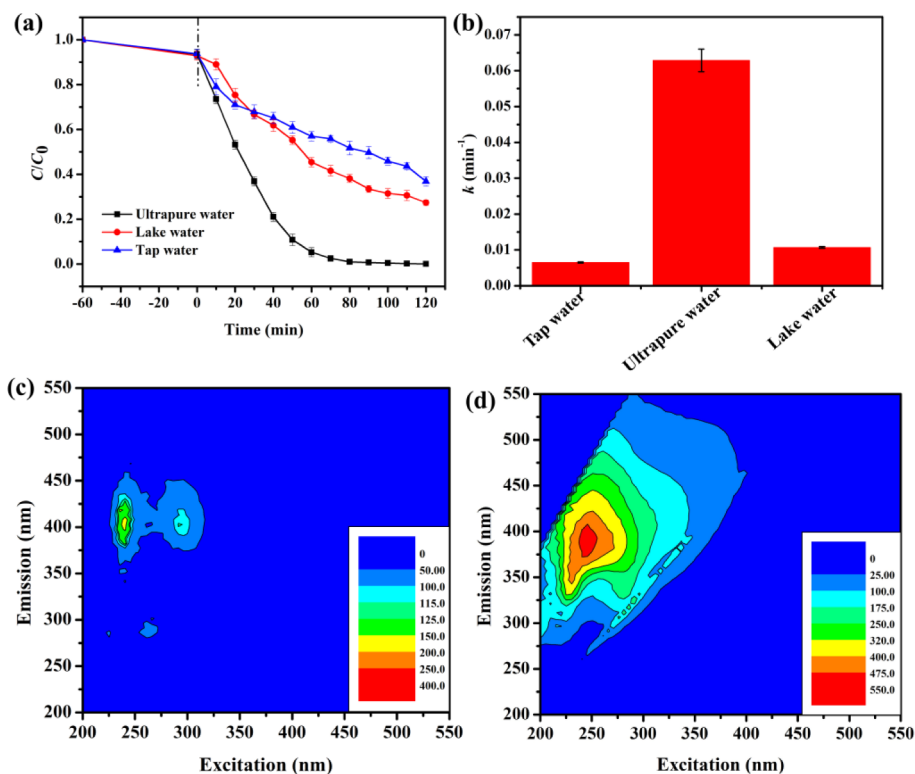


Fig. 8. (a) Effect on light intensity variation on Cr(VI) removal and (b) light intensity versus  $k$  values,  $r^2 = 0.82$ . Conditions: BB-100 = 50 mg, Cr(VI) = 10 mg/L, 200 mL,  $\text{pH} = 2.0$ .





**Fig. 9.** (a) Effect on water matrix variation on Cr(VI) removal and (b) their corresponding  $k$  values, (c) and (d) excitation-emission matrix spectra of tap water and lake water used in this study.

referred to the humic-like components such as humic acid (HA) or fulvic acid (FA) [94,95]. Because the maximum fluorescence intensity of humic-like components in lake water (547 QSU) was much higher than that in tap water (178 QSU), therefore the abundant HA or FA molecules can serve as electron donor to scavenge the photo-generated holes [96,97], resulting in suppressing electron-hole recombination and promoting the photocatalytic reduction of Cr(VI) ions.

In order to verify the above conjecture, the Box-Behnken experimental design methodology was used to further study the effects of co-existing matters on the photoreduction process. It was believed that the inorganic cations ( $K^+$ ,  $Na^+$ ,  $Ca^{2+}$  and  $Mg^{2+}$ ) existed in two water matrices might not influence the photoreduction process distinctly due to that they can't consume the photo-induced electrons or holes resulting from the stable and highest oxidation states [98]. As shown in Table S3, the effect of 4 experimental variables, namely the concentration of  $Cl^-$  (A),  $NO_3^-$  (B),  $SO_4^{2-}$  (C) and DOM (D) on the photocatalytic efficiency of Cr(VI) removal was investigated. Table S4 (4 factors and 29 runs) exhibited the results of analysis of variables for the photoreduction efficiency of Cr(VI) using BB-100 under white light irradiation. Meanwhile, a quadratic polynomial model was obtained to predict the relationship between the response (photocatalytic efficiency %) and independent variable, as expressed in Eq. (4).

$$\begin{aligned} \text{Efficiency \%} = & 80.80 - 3.25A - 0.25B - 7.58C + 9.25D + 2.50AB \\ & - 1.00AC + 0.75AD + 5.00BC - 0.75BD - 0.25CD \\ & - 2.98A^2 - 0.48B^2 - 2.73C^2 - 4.98D^2 \end{aligned} \quad (4)$$

Table S5 listed the results of ANOVA for the photoreduction efficiency of Cr(VI) using BB-100 under white light irradiation. Significant parameter of this model was  $< 0.0001$ , and the  $r^2$  and  $r^2_{\text{adjusted}}$  values were 0.98 and 0.96, respectively, indicating that the experimental data can highly describe the proposed model obtained by the Box-Behnken response surface methodology. Besides, according to the  $F$ -values of variables, it can be concluded that the influence of 4 variables on Cr(VI) reduction fitted the following order:  $D > C > A > B$ . This result

indicated that the presence of DOM,  $SO_4^{2-}$  and  $Cl^-$  had remarkable impact on photoreduction efficiency. Since the concentration range of  $NO_3^-$  was relatively narrow, so the corresponding input values had little effect on the final output values. Moreover, to investigate the interaction between the above-stated variables, three-dimensional surfaces plots were shown in Fig. 10. It can be seen that the photoreduction efficiency decreased with increase in the concentration of inorganic anions, especially for  $SO_4^{2-}$ . This was because  $SO_4^{2-}$  ions were doubly charged and its adsorption capacity on the BB-100 at acid medium was stronger than that of  $Cl^-$  and  $NO_3^-$  [98]. Additionally, the increasing of DOM concentration showed a positively significant effect on photoreduction efficiency. The optimum efficiency was fitted by the Box-Behnken methodology with the initial concentrations of  $Cl^-$ ,  $NO_3^-$ ,  $SO_4^{2-}$  and DOM were 36.4, 9.5, 76.3 and 10.5 mg/L, respectively. Based on the above experimental and theoretical results, it can be concluded that the photoreduction efficiency of Cr(VI) using BB-100 under acid medium was inclined to decrease with the presence of co-existing inorganic anions and to increase with the presence of DOM.

### 3.2.5. Photocatalytic activity under real sunlight

Real sunlight irradiation is a safe, cost-effective and sustainable energy source for photocatalytic Cr(VI) reduction. In this study, photoreduction of Cr(VI) over BB-100 under real sunlight in a field experiment was also carried out. To test the photocatalytic performance of BB-100 under real sunlight irradiation, photoreduction of Cr(VI) was performed at Daxing campus of BUCEA (39°44' N, 116°17'E) in the spring (April 22, 2019, labeled as real sunlight-1) and autumn season (September 26th and 29th, 2019, labeled as real sunlight-2 and real sunlight-3, respectively) under the identical condition of 0.5 g/L photocatalyst, 10 mg/L Cr(VI) solution and pH being 2.0. The spectrum of real sunlight and experimental devices were illustrated in Figs. S2 and S3. As shown in Fig. 11(a), it can be observed that only 12.3% and 15.9% of Cr(VI) ions were removed by self-reduction and adsorption after 180 min. Being compared with the white light irradiation, the

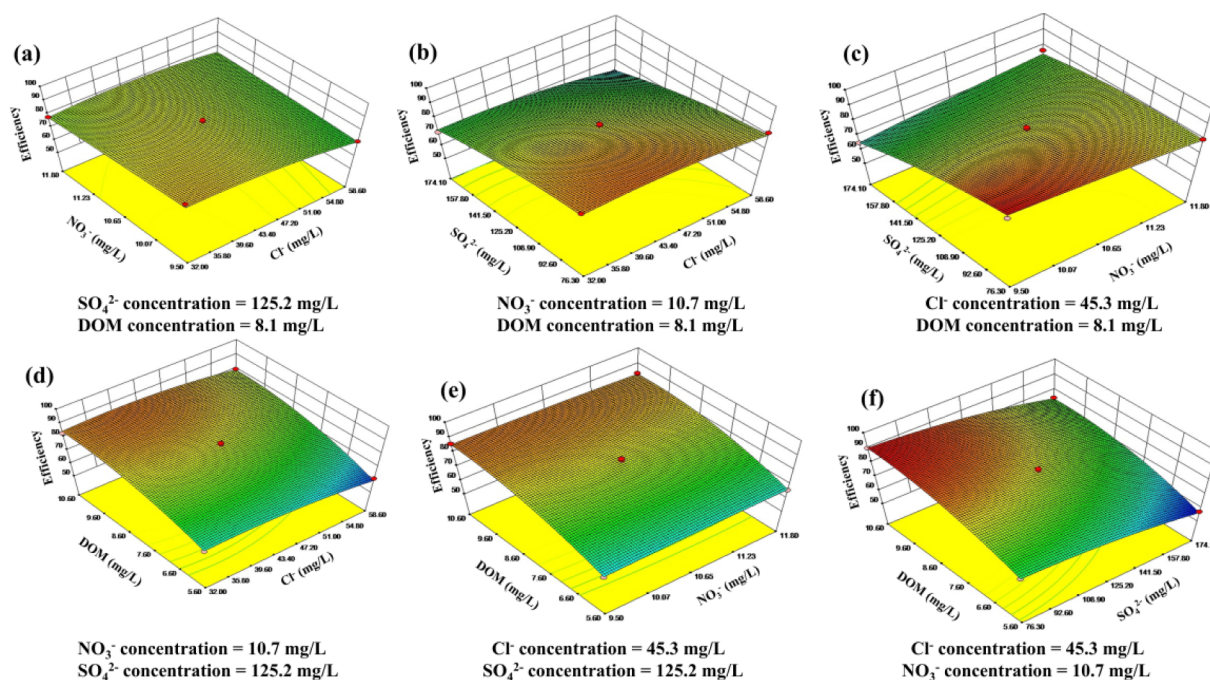


Fig. 10. Response surface graphs of effects of concentrations of  $\text{Cl}^-$ ,  $\text{NO}_3^-$ ,  $\text{SO}_4^{2-}$  and DOM on the photocatalytic efficiency of Cr(VI) reduction using BB-100 under pH = 2.

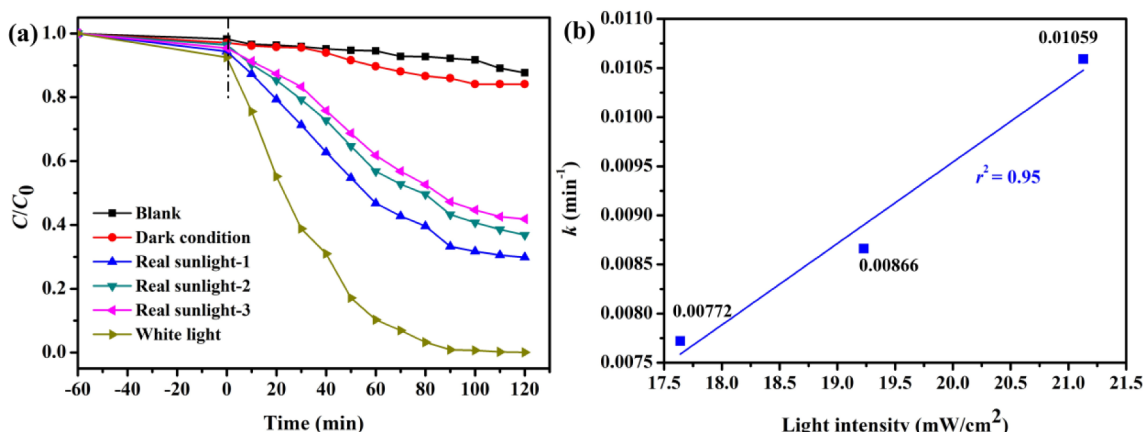


Fig. 11. (a) Photoreduction of Cr(VI) under different light sources and (b) real sunlight intensity versus  $k$  values,  $r^2 = 0.95$ . Conditions: BB-100 = 50 mg, Cr (VI) = 10 mg/L, 200 mL, pH = 2.0.

photocatalytic efficiencies decreased to 70.1%, 63.1% and 58.1% for the real sunlight-1, real sunlight-2 and real sunlight-3, respectively. The reason for this phenomenon is probably ascribed to the weaker sunlight intensity on the day of the experiment, the average intensities of real sunlight-1, real sunlight-2 and real sunlight-3 were 21.13, 19.23 and 17.64  $\text{mW}/\text{cm}^2$ , which were much lower than the white light intensity under the optimal experimental condition (approximately 46.07  $\text{mW}/\text{cm}^2$ ), thus limiting its photocatalytic activity. As shown in Fig. 11(b), there was a significant positive correlation between real sunlight intensity and  $k$  values ( $r^2 = 0.95$ ), indicating that the illumination intensity is the dominating factor of Cr(VI) photoreduction.

### 3.3. Reusability and stability of BUC-21/ $\text{Bi}_{24}\text{O}_{31}\text{Br}_{10}$ composites

As illustrated in Fig. 12(a), the photocatalytic reduction activities of Cr(VI) were compared by BB-100 and  $\text{Bi}_{24}\text{O}_{31}\text{Br}_{10}$  over 4 continuous cycles.  $\text{Bi}_{24}\text{O}_{31}\text{Br}_{10}$  showed inferior photocatalytic activity, a total removal of 34.2% at 120 min even in the first cycle and only 23.8% of Cr (VI) can be removed after 4 cycles. However, 83.1% of Cr(VI) can be

photoreduced after 4 cycling experiments, suggesting that the BB-100 had reasonable good recyclability during the adsorption-photocatalysis experiments. Being compared to the photocatalytic efficiency of the first cyclic experiment, a credible interpretation of the slight decrease of Cr(VI) removal after 4-run cycling experiments was fact that a small amount of Cr(VI) or Cr(III) inorganic ions might be absorbed on the surface or in the pores of BB-100. To confirm the reduction of Cr(VI) to Cr(III), XPS tests were carried out to explore the chemical state of Cr on BB-100 after photocatalysis. The survey XPS spectra showed the presence of Cr signals after cyclic experiments (Fig. 12(b)). The high resolution of Cr 2p spectrum was depicted in Fig. 12(c). Cr 2p spectrum can be curve-fitted with two peaks at 577.4 and 587.1 eV, respectively, revealing that Cr(VI) was reduced to Cr(III) [99]. Furthermore, because the potential of Bi(III)/Bi is 0.308 V vs NHE [100], so the  $\text{Bi}^{3+}$  can be easily reduced by the photo-generated electrons during the cyclic photocatalytic process, which might also reduce the photocatalytic efficiency for Cr(VI) removal. In this study, the Bi and Zn ions leached out to the solution after the 4 cyclic experiments were found to be  $21 \pm 0.5$  mg/L and  $19 \pm 0.6$  mg/L, respectively. However, the PXRD

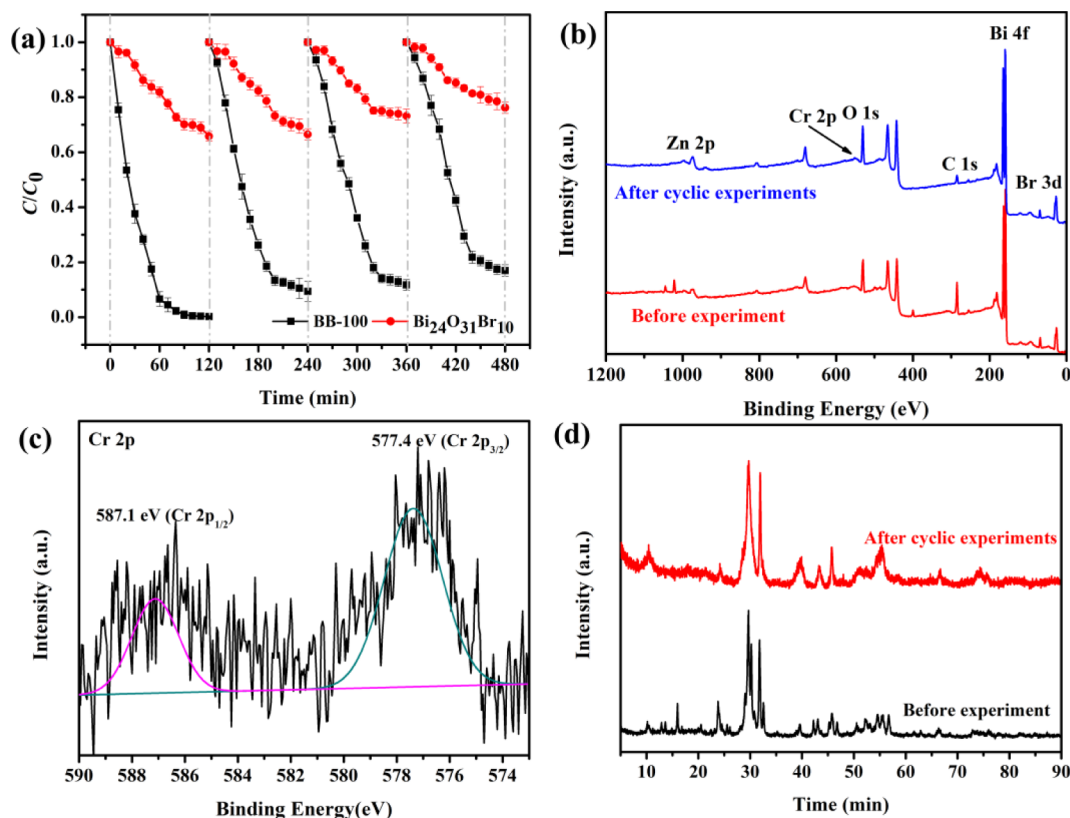


Fig. 12. (a) Recycling tests for the Cr(VI) photoreduction over BB-100 and Bi<sub>24</sub>O<sub>31</sub>Br<sub>10</sub>, (b) XPS survey spectra of BB-100 before and after the photocatalytic reaction, (c) Cr 2p spectrum of BB-100 after the cyclic experiments and (d) PXRD patterns of BB-100 before and after Cr(VI) reduction experiments.

patterns (Fig. 12(d)), SEM images (Figs. S4(a)–(b)) and TEM images (Fig. S4(c)–(d)) before and after photocatalysis showed that the BB-100 basically remained its original phase composition and morphology, indicating that metals leaching may not play significant role in the photocatalytic efficiency.

### 3.4. Possible photocatalytic mechanism

Photoluminescence (PL) spectrometer is diffusely applied to study the separation efficiency of the photo-generated carriers. Lower PL signals suggest higher separation efficiency for the photo-generated carriers [101,102]. As illustrated in Fig. 13(a), it can be found that the PL intensity followed the order of BUC-21 > Bi<sub>24</sub>O<sub>31</sub>Br<sub>10</sub> > BB-25 > BB-50 > BB-75 > BB-150 > BB-125 > BB-100, indicating that BB-100 exhibited better charge carrier separation than the individual Bi<sub>24</sub>O<sub>31</sub>Br<sub>10</sub>, BUC-21 and the other BB-x composites. Moreover, the photo-generated carrier separation performance was further affirmed by EIS and photocurrent determination. It was obvious that the diameter of arc radius also followed the order of BUC-21 > Bi<sub>24</sub>O<sub>31</sub>Br<sub>10</sub> > BB-25 > BB-50 > BB-75 > BB-150 > BB-125 > BB-100 (Fig. 13(b)), confirming that BB-100 exhibited stronger charge separation or interfacial charge transfer ability than the other photocatalysts [103–105]. Additionally, the photocurrent-time curves for the above photocatalysts were displayed in Fig. 13(c). It can be seen that BB-100 possessed better photocurrent response than that of BUC-21 and Bi<sub>24</sub>O<sub>31</sub>Br<sub>10</sub>, suggesting that the formation of composites between the BUC-21 and Bi<sub>24</sub>O<sub>31</sub>Br<sub>10</sub> could suppress the photo-generated electron-hole pair recombination. Additionally, the time-resolved photoluminescence analysis was carried out to further understand the more information of the charge carriers. As shown in Fig. 13(d), it can be seen that the average PL lifetime ( $\tau_{\text{average}}$ ) of the BB-100 was 3.49 ns, which was larger than pure BUC-21 (2.86 ns) and Bi<sub>24</sub>O<sub>31</sub>Br<sub>10</sub> (0.41 ns). Previous studies had demonstrated that a longer PL lifetime meant lower

recombination rate of photo-generated electron-hole pairs [106,107]. Therefore, the larger PL lifetime of BB-100 also proved its better charge separation capacity and thus the higher photocatalytic efficiency.

The manner of photoreduction performance improvement of the BB-100 composites can be ascertained by their band positions. As illustrated in Fig. 13(e) and 13(f), the slope of linear  $C^{2-}$  potential curves of BUC-21 and Bi<sub>24</sub>O<sub>31</sub>Br<sub>10</sub> were positive, indicating that they possessed the property of n-typed semiconductor [108]. The flat-band potentials ( $E_{\text{FB}}$ ) of Bi<sub>24</sub>O<sub>31</sub>Br<sub>10</sub> and BUC-21 were approximately  $-0.79$  and  $-1.43$  eV vs the Ag/AgCl electrode, respectively. With respect to the most of n-typed semiconductor, the  $E_{\text{FB}}$  is more positive 0.1 eV than the conduction band potential ( $E_{\text{CB}}$ ) [109], therefore, the  $E_{\text{CB}}$  of Bi<sub>24</sub>O<sub>31</sub>Br<sub>10</sub> and lowest unoccupied molecular orbital (LUMO) of BUC-21 were  $-0.69$  and  $-1.33$  eV vs NHE, respectively [30,37,60]. Combining the  $E_{\text{g}}$  values calculated from UV-vis DRS spectra and the theoretical equation of  $E_{\text{g}} = E_{\text{VB}} - E_{\text{CB}}$ , the valence band potential ( $E_{\text{VB}}$ ) of Bi<sub>24</sub>O<sub>31</sub>Br<sub>10</sub> and the highest occupied molecular orbital (HOMO) of BUC-21 were accounted to be 1.96 and 2.14 eV, respectively.

Based on the obtained experimental results, the possible reaction mechanism was illustrated in Fig. 14(a). During the photocatalytic process, both BUC-21 and Bi<sub>24</sub>O<sub>31</sub>Br<sub>10</sub> can be excited by the white light to produce photoelectrons and holes. The photo-generated electrons can migrate from the LUMO of BUC-21 to the CB of Bi<sub>24</sub>O<sub>31</sub>Br<sub>10</sub>, because of the difference between the  $E_{\text{LUMO}}/E_{\text{CB}}$  of BUC-21 and Bi<sub>24</sub>O<sub>31</sub>Br<sub>10</sub> at  $-1.33$  and  $-0.69$  eV, respectively. As the redox potential of Cr(VI)/Cr(III) is 1.35 eV vs NHE (pH = 0) [87,110], hence the Cr(VI) was inclined to effectually photoreduced into Cr(III) by the accumulated electrons in the CB of Bi<sub>24</sub>O<sub>31</sub>Br<sub>10</sub> under the acidic conditions. Meanwhile, the photo-generated holes were consumed by H<sub>2</sub>O to produce H<sub>2</sub>O<sub>2</sub> [111]. Notably, since the redox potential value of O<sub>2</sub>/O<sub>2</sub><sup>•−</sup> at  $-0.33$  eV was lower than  $E_{\text{LUMO}}/E_{\text{CB}}$  of BUC-21 and Bi<sub>24</sub>O<sub>31</sub>Br<sub>10</sub> [112], so the dissolved O<sub>2</sub> can react with photo-generated electrons to produce 'O<sub>2</sub><sup>•−</sup> both in the LUMO/CB of BUC-21 and

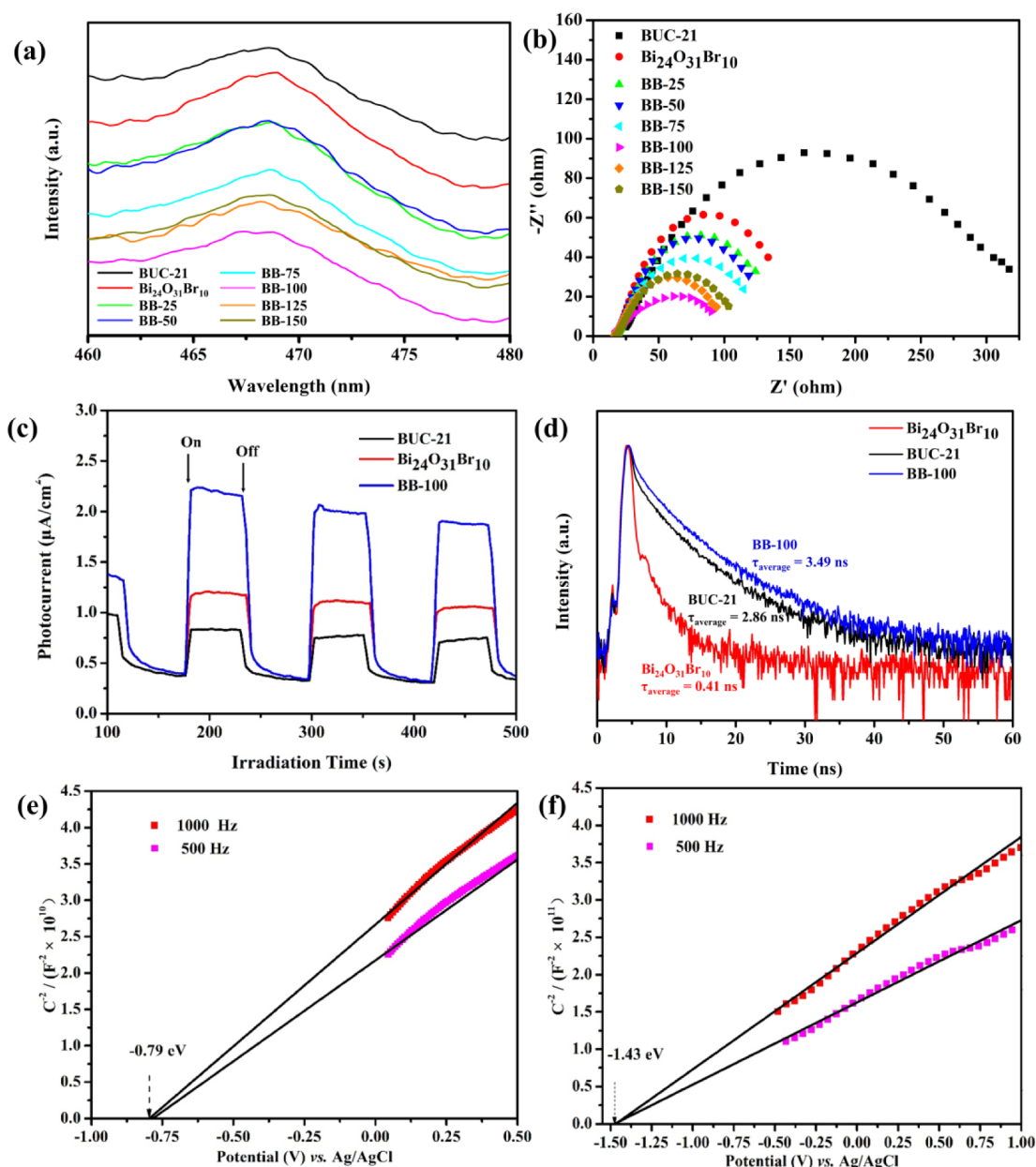
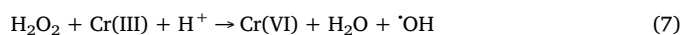
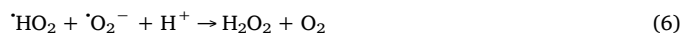


Fig. 13. (a) Photoluminescence spectra, (b) EIS Nyquist plots (c) photocurrent response density and (d) time-resolved PL decay spectra of BUC-21, BB-100 and Bi<sub>24</sub>O<sub>31</sub>Br<sub>10</sub>. Mott-Schottky curves of (e) Bi<sub>24</sub>O<sub>31</sub>Br<sub>10</sub> and (f) BUC-21 at different frequency.

Bi<sub>24</sub>O<sub>31</sub>Br<sub>10</sub>, respectively. As illustrated in Fig. 14(b), notable signals of DMPO- $\cdot\text{O}_2^-$  were detected on electron spin resonance (ESR) after the white light irradiation for 5 and 10 min, suggesting  $\cdot\text{O}_2^-$  radicals were really generated during the photocatalysis. This process might induce a  $\cdot\text{O}_2^-$ -mediated Cr(VI) photoreduction, thus enhancing the separation efficiency of the electron-hole pairs and promoting the removal of Cr(VI) [17,86,112,113].

Radical quenching experiments were also carried out to identify the contribution of active species involved in the BB-100 system. KBrO<sub>3</sub> and *p*-benzoquinone (BQ) were used as scavengers to quench the photo-generated electrons and  $\cdot\text{O}_2^-$ , respectively [114,115]. While the  $\cdot\text{OH}$  and  $\text{h}^+$  can be captured by *t*-butanol (TBA) and EDTA-2Na, respectively [102,115]. As shown in Fig. 14(c), the reduction efficiency of Cr(VI) decreased markedly with the addition of KBrO<sub>3</sub>, implying that the dominant role of  $\text{e}^-$  in photocatalytic reaction. In the presence of BQ, a moderate decrease of the Cr(VI) photoreduction efficiency can be observed, indicating that  $\cdot\text{O}_2^-$  was also responsible for Cr(VI) reduction,

which was consistent with the ESR analysis. It was worthy to nothing that the presence of TBA resulted in a sharp drop in the photocatalytic reduction of Cr(VI) by BB-100. This phenomenon can be attributed to the equilibrium shifting toward Cr(VI) as listed in the following Eqs. (5)–(7). The addition of EDTA-2Na triggered a fierce promotion of Cr(VI) reduction, suggesting that  $\text{h}^+$  capture was beneficial to the separation of photo-generated electrons, thus improving the photocatalytic efficiency.



Additionally, the DFT calculation was used to further explore the interactions between the BUC-21 and Bi<sub>24</sub>O<sub>31</sub>Br<sub>10</sub>. As illustrated in Fig. S5, it can be observed that the most stable structure of Bi<sub>24</sub>O<sub>31</sub>Br<sub>10</sub> on BUC-21 surface after geometry relaxation. An obvious reconstruction



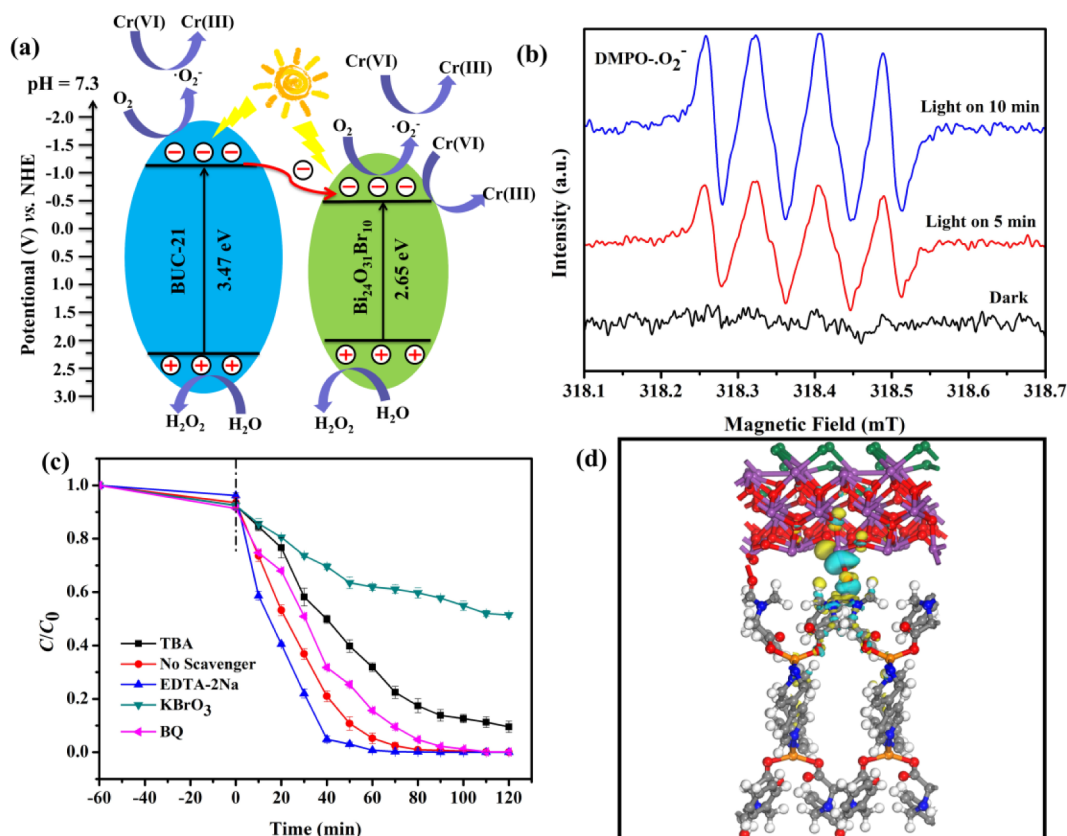


**Fig. 14.** (a) Illustration of plausible mechanism of photocatalysis reduction of Cr(VI) over BB-100 under white light, (b) ESR spectra of radical adducts trapped by DMPO-O<sub>2</sub><sup>•-</sup> for BB-100 in the dark and under white light irradiation, (c) Reactive species trapping experiments of BB-100 under white light irradiation, (d) Electron density difference around BUC-21 surface and Bi<sub>24</sub>O<sub>31</sub>Br<sub>10</sub> fragment when Bi<sub>24</sub>O<sub>31</sub>Br<sub>10</sub> adsorbed on the BUC-21 surface from the side view. The orange, green, purple, blue, red, grey, white sphere presented Zn, Br, Bi, N, O, C and H atom respectively. (For interpretation of the references to color in this figure legend, the reader is referred to the web version of this article.)

both in the surface and adsorbate revealed a strong chemical interaction between Bi<sub>24</sub>O<sub>31</sub>Br<sub>10</sub> on BUC-21. Furthermore, this chemical interaction can also be proved by the electron density difference as shown in Fig. 14(d). The most prominent feature of the electron density difference was decline area (light blue) of electron density around the O atoms of BUC-21 surface and the increasing area (yellow) around Bi and O atoms of Bi<sub>24</sub>O<sub>31</sub>Br<sub>10</sub> fragment. Moreover, the Hirshfeld charge analysis [116] (Tables S6–S7) revealed that the negative charge of O atoms in Bi<sub>24</sub>O<sub>31</sub>Br<sub>10</sub> fragment in the adsorption process, suggesting that photo-generated electrons transferred from BUC-21 to Bi<sub>24</sub>O<sub>31</sub>Br<sub>10</sub>. Therefore, the above DFT simulation results matched perfectly the experimental results.

#### 4. Conclusions

In summary, the sheet-like Bi<sub>24</sub>O<sub>31</sub>Br<sub>10</sub> photocatalyst with the monoclinic phase was facilely synthesized by hydrothermal method. Furthermore, a series of BUC-21/Bi<sub>24</sub>O<sub>31</sub>Br<sub>10</sub> binary coupling composites were prepared using the facile ball-milling method, in which the BUC-21 served as the substrate for the establishment of composites. The results indicated that the BUC-21/Bi<sub>24</sub>O<sub>31</sub>Br<sub>10</sub> composites displayed improved photocatalytic performance for Cr(VI) removal under white light. In addition to the enhanced visible-light absorption, the synergistic effect was also attributed to the uniform coating of Bi<sub>24</sub>O<sub>31</sub>Br<sub>10</sub> on the surface of BUC-21 by ball-milling method, which provided strong chemical interface between the two components to achieve effective separation of the electron-hole pairs. The different SOAs, initial pH values, light intensities and the co-existing matters played significant roles in the photoreduction efficiency of Cr(VI) ions.

Furthermore, the cyclic experiments also showed that the prepared photocatalysts had reasonably good reusability and stability. This work might give us a new insight for fabrication of bismuth-rich Bi<sub>x</sub>O<sub>y</sub>X<sub>z</sub> (X = Br, Cl, I)/MOF hybrid photocatalysts with superior performance for remediation of the Cr-contaminated wastewater.

#### Declaration of Competing Interest

The authors declare that they have no known competing financial interests or personal relationships that could have appeared to influence the work reported in this paper.

#### Acknowledgement

This work was supported by the National Natural Science Foundation of China (21876008, 51578034 and 51878023), Great Wall Scholars Training Program Project of Beijing Municipality Universities (CIT&TCD20180323), Project of Construction of Innovation Teams and Teacher Career Development for Universities and Colleges Under Beijing Municipality (IDHT20170508), Beijing Talent Project (2018A35), the Fundamental Research Funds for Beijing Universities (X18075/X18076/X18124/X18125/X18276) and Scientific Research Foundation of Beijing University of Civil Engineering and Architecture (KYJJ2017033/KYJJ2017008).

#### Appendix A. Supplementary data

Supplementary data to this article can be found online at <https://doi.org/10.1016/j.cej.2019.123431>.

## References

- [1] J.J. Testa, M.A. Grela, M.I. Litter, Heterogeneous photocatalytic reduction of chromium(VI) over TiO<sub>2</sub> particles in the presence of oxalate: Involvement of Cr(V) species, *Environ. Sci. Technol.* 38 (2004) 1589–1594.
- [2] C.-C. Wang, X.-D. Du, J. Li, X.-X. Guo, P. Wang, J. Zhang, Photocatalytic Cr(VI) reduction in metal-organic frameworks: A mini-review, *Appl. Catal. B-Environ.* 193 (2016) 198–216.
- [3] J.-K. Yang, S.-M. Lee, Removal of Cr(VI) and humic acid by using TiO<sub>2</sub> photocatalysis, *Chemosphere* 63 (2006) 1677–1684.
- [4] Y. Xu, D. Zhao, Reductive immobilization of chromate in water and soil using stabilized iron nanoparticles, *Water Res.* 41 (2007) 2101–2108.
- [5] W.J. Jiang, Q. Cai, W. Xu, M.W. Yang, Y. Cai, D.D. Dionysiou, K.E. O'Shea, Cr(VI) adsorption and reduction by humic acid coated on magnetite, *Environ. Sci. Technol.* 48 (2014) 8078–8085.
- [6] I. Kretschmer, A.M. Senn, J.M. Meichtry, G. Custo, E.B. Halac, R. Dillert, D.W. Bahnemann, M.I. Litter, Photocatalytic reduction of Cr(VI) on hematite nanoparticles in the presence of oxalate and citrate, *Appl. Catal. B-Environ.* 242 (2019) 218–226.
- [7] M. Costa, Toxicity and carcinogenicity of Cr(VI) in animal models and humans, *Crit. Rev. Toxicol.* 27 (1997) 431–442.
- [8] L. Zhang, F. Fu, B. Tang, Adsorption and redox conversion behaviors of Cr(VI) on goethite/carbon microspheres and akaganeite/carbon microspheres composites, *Chem. Eng. J.* 356 (2019) 151–160.
- [9] H.-L. Ma, Y. Zhang, Q.-H. Hu, D. Yan, Z.-Z. Yu, M. Zhai, Chemical reduction and removal of Cr(VI) from acidic aqueous solution by ethylenediamine-reduced graphene oxide, *J. Mater. Chem.* 22 (2012) 5914–5916.
- [10] F. Deng, X.Y. Lu, Y.B. Luo, J. Wang, W.J. Che, R.J. Yang, X.B. Luo, S.L. Luo, D.D. Dionysiou, Novel visible-light-driven direct Z-scheme CdS/CuInS<sub>2</sub> nanoplates for excellent photocatalytic degradation performance and highly-efficient Cr(VI) reduction, *Chem. Eng. J.* 361 (2019) 1451–1461.
- [11] J. Hu, G. Chen, I.M.C. Lo, Removal and recovery of Cr(VI) from wastewater by maghemite nanoparticles, *Water Res.* 39 (2005) 4528–4536.
- [12] S.-H. Zhang, M.-F. Wu, T.-T. Tang, Q.-J. Xing, C.-Q. Peng, F. Li, H. Liu, X.-B. Luo, J.-P. Zou, X.-B. Min, J.-M. Luo, Mechanism investigation of anoxic Cr(VI) removal by nano zero-valent iron based on XPS analysis in time scale, *Chem. Eng. J.* 335 (2018) 945–953.
- [13] Y. Tian, L. Huang, X. Zhou, C. Wu, Electroreduction of hexavalent chromium using a polypyrrole-modified electrode under potentiostatic and potentiodynamic conditions, *J. Hazard. Mater.* 225–226 (2012) 15–20.
- [14] Y. Yang, M.H. Diao, M.M. Gao, X.F. Sun, X.W. Liu, G.H. Zhang, Z. Qi, S.G. Wang, Facile preparation of graphene/polyaniline composite and its application for electrocatalysis hexavalent chromium reduction, *Electrochim. Acta* 132 (2014) 496–503.
- [15] A.U. Chaudhari, S.R. Tapase, V.L. Markad, K.M. Kodam, Simultaneous decolorization of reactive Orange M2R dye and reduction of chromate by *Lysinibacillus* sp. KMK-A, *J. Hazard. Mater.* 262 (2013) 580–588.
- [16] J. Chung, R. Nerenberg, B.E. Rittmann, Bio-reduction of soluble chromate using a hydrogen-based membrane biofilm reactor, *Water Res.* 40 (2006) 1634–1642.
- [17] F. Zhang, Y.C. Zhang, G.S. Zhang, Z.J. Yang, D.D. Dionysiou, A.P. Zhu, Exceptional synergistic enhancement of the photocatalytic activity of SnS<sub>2</sub> by coupling with polyaniline and N-doped reduced graphene oxide, *Appl. Catal. B-Environ.* 236 (2018) 53–63.
- [18] K. Li, Z. Huang, S. Zhu, S. Luo, L. Yan, Y. Dai, Y. Guo, Y. Yang, Removal of Cr(VI) from water by a biochar-coupled g-C<sub>3</sub>N<sub>4</sub> nanosheets composite and performance of a recycled photocatalyst in single and combined pollution systems, *Appl. Catal. B-Environ.* 243 (2019) 386–396.
- [19] M. Feng, P. Zhang, H.-C. Zhou, V.K. Sharma, Water-stable metal-organic frameworks for aqueous removal of heavy metals and radionuclides: a review, *Chemosphere* 209 (2018) 783–800.
- [20] Y. Shu, C.X. Wang, Y.C. Zhang, Z.J. Yang, D.D. Dionysiou, Design and preparation of SnO<sub>2</sub>/SnS<sub>2</sub>/conjugated polyvinyl chloride derivative ternary composite with enhanced visible-light photocatalytic activity, *Mater. Res. Bull.* 118 (2019) 110524–110533.
- [21] C.-C. Wang, Y.-Q. Zhang, J. Li, P. Wang, Photocatalytic CO<sub>2</sub> reduction in metal-organic frameworks: a mini review, *J. Mol. Struct.* 1083 (2015) 127–136.
- [22] C.-C. Wang, J.-R. Li, X.-L. Lv, Y.-Q. Zhang, G. Guo, Photocatalytic organic pollutants degradation in metal-organic frameworks, *Energ. Environ. Sci.* 7 (2014) 2831–2867.
- [23] Q. Zhang, J. Yu, J. Cai, L. Zhang, Y. Cui, Y. Yang, B. Chen, G. Qian, A porous Zr-cluster-based cationic metal-organic framework for highly efficient Cr<sub>2</sub>O<sub>7</sub><sup>2-</sup> removal from water, *Chem. Commun.* 51 (2015) 14732–14734.
- [24] T. Zhang, W. Lin, Metal-organic frameworks for artificial photosynthesis and photocatalysis, *Chem. Soc. Rev.* 43 (2014) 5982–5993.
- [25] A. Dhakshinamoorthy, A.M. Asiri, H. Garcia, Metal-organic framework (MOF) compounds: Photocatalysts for redox reactions and solar fuel production, *Angew. Chem. Int. Edit.* 55 (2016) 5414–5445.
- [26] B. Aguila, Q. Sun, X. Wang, E. O'Rourke, A.M. Al-Enizi, A. Nafady, S. Ma, Lower activation energy for catalytic reactions through host-guest cooperation within metal-organic frameworks, *Angew. Chem. Int. Edit.* 57 (2018) 10107–10111.
- [27] H.-P. Jing, C.-C. Wang, Y.-W. Zhang, P. Wang, R. Li, Photocatalytic degradation of methylene blue in ZIF-8, *RSC Adv.* 4 (2014) 54454–54462.
- [28] L. Shen, S. Liang, W. Wu, R. Liang, L. Wu, Multifunctional NH<sub>2</sub>-mediated zirconium metal-organic framework as an efficient visible-light-driven photocatalyst for selective oxidation of alcohols and reduction of aqueous Cr(VI), *Dalton. T.* 42 (2013) 13649–13657.
- [29] L. Shen, W. Wu, R. Liang, R. Lin, L. Wu, Highly dispersed palladium nanoparticles anchored on UiO-66(NH<sub>2</sub>) metal-organic framework as a reusable and dual functional visible-light-driven photocatalyst, *Nanoscale* 5 (2013) 9374–9382.
- [30] X.-D. Du, X.-H. Yi, P. Wang, W. Zheng, J. Deng, C.-C. Wang, Robust photocatalytic reduction of Cr(VI) on UiO-66-NH<sub>2</sub>(Zr/Hf) metal-organic framework membrane under sunlight irradiation, *Chem. Eng. J.* 356 (2019) 393–399.
- [31] D. Sun, L. Ye, Z. Li, Visible-light-assisted aerobic photocatalytic oxidation of amines to imines over NH<sub>2</sub>-MIL-125(Ti), *Appl. Catal. B-Environ.* 164 (2015) 428–432.
- [32] H. Wang, X. Yuan, Y. Wu, G. Zeng, X. Chen, L. Leng, Z. Wu, L. Jiang, H. Li, Facile synthesis of amino-functionalized titanium metal-organic frameworks and their superior visible-light photocatalytic activity for Cr(VI) reduction, *J. Hazard. Mater.* 286 (2015) 187–194.
- [33] M. Bagheri, M.Y. Masoomi, A. Morsali, A MoO<sub>3</sub>-metal-organic framework composite as a simultaneous photocatalyst and catalyst in the PODS process of light oil, *ACS Catal.* 7 (2017) 6949–6956.
- [34] M.Y. Masoomi, M. Bagheri, A. Morsali, High efficiency of mechanosynthesized Zn-based metal-organic frameworks in photodegradation of congo red under UV and visible light, *RSC Adv.* 6 (2016) 13272–13277.
- [35] M.Y. Masoomi, M. Bagheri, A. Morsali, P.C. Junk, High photodegradation efficiency of phenol by mixed-metal-organic frameworks, *Inorg. Chem. Front.* 3 (2016) 944–951.
- [36] F.-X. Wang, X.-H. Yi, C.-C. Wang, J.-G. Deng, Photocatalytic Cr(VI) reduction and organic-pollutant degradation in a stable 2D coordination polymer, *Chinese J. Catal.* 38 (2017) 2141–2149.
- [37] X.-H. Yi, F.-X. Wang, X.-D. Du, P. Wang, C.-C. Wang, Facile fabrication of BUC-21/g-C<sub>3</sub>N<sub>4</sub> composites and their enhanced photocatalytic Cr(VI) reduction performances under simulated sunlight, *Appl. Organomet. Chem.* 33 (2019) 4621–4632.
- [38] S. Wang, X. Wang, Multifunctional metal-organic frameworks for photocatalysis, *Small* 11 (2015) 3097–3112.
- [39] L. Zeng, X. Guo, C. He, C. Duan, Metal-organic frameworks: Versatile materials for heterogeneous photocatalysis, *ACS Catal.* 6 (2016) 7935–7947.
- [40] W. Zhang, J.J. Dynes, Y. Hu, P. Jiang, S. Ma, Porous metal-metalloporphyrin gel as catalytic binding pocket for highly efficient synergistic catalysis, *Nature Commun.* 10 (2019) 1913.
- [41] X. Wang, J. Liu, S. Leong, X. Lin, J. Wei, B. Kong, Y. Xu, Z.-X. Low, J. Yao, H. Wang, Rapid construction of ZnO@ZIF-8 heterostructures with size-selective photocatalysis properties, *ACS Appl. Mater. Inter.* 8 (2016) 9080–9087.
- [42] J. Qiu, X. Zhang, Y. Feng, X. Zhang, H. Wang, J. Yao, Modified metal-organic frameworks as photocatalysts, *Appl. Catal. B-Environ.* 231 (2018) 317–342.
- [43] J. Ding, Z. Yang, C. He, X. Tong, Y. Li, X. Niu, H. Zhang, UiO-66(Zr) coupled with Bi<sub>2</sub>MoO<sub>6</sub> as photocatalyst for visible-light promoted dye degradation, *J. Colloid Interf. Sci.* 497 (2017) 126–133.
- [44] S.-R. Zhu, P.-F. Liu, M.-K. Wu, W.-N. Zhao, G.-C. Li, K. Tao, F.-Y. Yi, L. Han, Enhanced photocatalytic performance of BiOBr/NH<sub>2</sub>-MIL-125(Ti) composite for dye degradation under visible light, *Dalton. T.* 45 (2016) 17521–17529.
- [45] F. Guo, H. Yang, L. Liu, Y. Han, A.M. Al-Enizi, A. Nafady, P.E. Kruger, S.G. Telfer, S. Ma, Hollow capsules of doped carbon incorporating metal@metal sulfide and metal@metal oxide core-shell nanoparticles derived from metal-organic framework composites for efficient oxygen electrocatalysis, *J. Mater. Chem. A* 7 (2019) 3624–3631.
- [46] X. Meng, Z. Zhang, Bismuth-based photocatalytic semiconductors: Introduction, challenges and possible approaches, *J. Mol. Catal. A-Chem.* 423 (2016) 533–549.
- [47] M. Li, H. Huang, S. Yu, N. Tian, Y. Zhang, Facet, junction and electric field engineering of bismuth-based materials for photocatalysis, *ChemCatChem* 10 (2018) 4477–4496.
- [48] Y. Wang, W. Jiang, W. Luo, X. Chen, Y. Zhu, Ultrathin nanosheets g-C<sub>3</sub>N<sub>4</sub>@Bi<sub>2</sub>WO<sub>6</sub> core-shell structure via low temperature reassembly strategy to promote photocatalytic activity, *Appl. Catal. B-Environ.* 237 (2018) 633–640.
- [49] D. Liu, W. Cai, Y. Wang, Y. Zhu, Constructing a novel Bi<sub>2</sub>SiO<sub>5</sub>/BiPO<sub>4</sub> heterostructure with extended light response range and enhanced photocatalytic performance, *Appl. Catal. B-Environ.* 236 (2018) 205–211.
- [50] J. Shang, W. Hao, X. Lv, T. Wang, X. Wang, Y. Du, S. Dou, T. Xie, D. Wang, J. Wang, Bismuth oxybromide with reasonable photocatalytic reduction activity under visible light, *ACS Catal.* 4 (2014) 954–961.
- [51] X. Xiao, R. Hu, C. Liu, C. Xing, X. Zuo, J. Nan, L. Wang, Facile microwave synthesis of novel hierarchical Bi<sub>2</sub>O<sub>3</sub>Br<sub>10</sub> nanoflakes with excellent visible light photocatalytic performance for the degradation of tetracycline hydrochloride, *Chem. Eng. J.* 225 (2013) 790–797.
- [52] Z. Liu, J. Liu, Z. Liu, J. Niu, P. Feng, Soluble starch-modulated solvothermal synthesis of grain-like Bi<sub>2</sub>O<sub>3</sub>Br<sub>10</sub> hierarchical architectures with enhanced photocatalytic activity, *Mater. Res. Bull.* 81 (2016) 119–126.
- [53] X. Xiao, C. Zheng, M. Lu, L. Zhang, F. Liu, X. Zuo, J. Nan, Deficient Bi<sub>2</sub>O<sub>3</sub>Br<sub>10</sub> as a highly efficient photocatalyst for selective oxidation of benzyl alcohol into benzaldehyde under blue LED irradiation, *Appl. Catal. B-Environ.* 228 (2018) 142–151.
- [54] J. Song, L. Zhang, J. Yang, X.-H. Huang, J.-S. Hu, Hierarchical porous Bi<sub>2</sub>O<sub>3</sub>Br<sub>10</sub> microarchitectures assembled by ultrathin nanosheets with strong adsorption and excellent photocatalytic performances, *Mater. Design* 123 (2017) 128–136.
- [55] X. Lou, J. Shang, L. Wang, H. Feng, W. Hao, T. Wang, Y. Du, Enhanced photocatalytic activity of Bi<sub>2</sub>O<sub>3</sub>Br<sub>10</sub>: Constructing heterojunction with BiOI, *J. Mater. Sci. Technol.* 33 (2017) 281–284.
- [56] J. Zhang, G. Cao, H. Wang, P. Feng, Z. Liu, Graphene-Bi<sub>2</sub>O<sub>3</sub>Br<sub>10</sub> composites with tunable architectures for enhanced photocatalytic activity and mechanism, *Ceram. Int.* 42 (2016) 11796–11804.

- [57] Z. He, Y. Xia, J. Su, B. Tang, Fabrication of magnetically separable  $\text{NiFe}_2\text{O}_4/\text{Bi}_2\text{O}_3/\text{Br}^-$  0 nanocomposites and excellent photocatalytic performance under visible light irradiation, *Opt. Mater.* 88 (2019) 195–203.
- [58] D. Liu, W. Yao, J. Wang, Y. Liu, M. Zhang, Y. Zhu, Enhanced visible light photocatalytic performance of a novel heterostructured  $\text{Bi}_2\text{O}_3/\text{Br}^-$  2/ $\text{Bi}_2\text{O}_3/\text{Br}^-$  0/ $\text{Bi}_2\text{SiO}_5$  photocatalyst, *Appl. Catal. B-Environ.* 172–173 (2015) 100–107.
- [59] X. Wang, W. Liu, H. Fu, X.-H. Yi, P. Wang, C. Zhao, C.-C. Wang, W. Zheng, Simultaneous Cr(VI) reduction and Cr(III) removal of bifunctional MOF/Titanate nanotube composites, *Environ. Pollut.* 249 (2019) 502–511.
- [60] X. Du, X. Yi, P. Wang, J. Deng, C.-C. Wang, Enhanced photocatalytic Cr(VI) reduction and diclofenac sodium degradation under simulated sunlight irradiation over MIL-100(Fe)/g- $\text{C}_3\text{N}_4$  heterojunctions, *Chinese J. Catal.* 40 (2019) 70–79.
- [61] S. Fang, S. Xue, C. Wang, G. Wang, X. Wang, Q. Liang, Z. Li, S. Xu, Fabrication and characterization of  $\text{CdS}/\text{BiVO}_4$  nanocomposites with efficient visible light driven photocatalytic activities, *Ceram. Int.* 42 (2016) 4421–4428.
- [62] Z. Yang, J. Ding, J. Feng, C. He, Y. Li, X. Tong, X. Niu, H. Zhang, Preparation of  $\text{BiVO}_4/\text{MIL}-125(\text{Ti})$  composite with enhanced visible-light photocatalytic activity for dye degradation, *Appl. Organomet. Chem.* 32 (2018) 4285–4295.
- [63] H. Zou, M. Song, F. Yi, L. Bian, P. Liu, S. Zhang, Simulated-sunlight-activated photocatalysis of methyl orange using carbon and lanthanum co-doped  $\text{Bi}_2\text{O}_3\text{-TiO}_2$  composite, *J. Alloy. Compd.* 680 (2016) 54–59.
- [64] P. Chen, F. Wang, Q. Zhang, Y. Su, L. Shen, K. Yao, Z.-F. Chen, Y. Liu, Z. Cai, W. Lv, G. Liu, Photocatalytic degradation of clofibric acid by g- $\text{C}_3\text{N}_4/\text{P25}$  composites under simulated sunlight irradiation: The significant effects of reactive species, *Chemosphere* 172 (2017) 193–200.
- [65] F. Meng, X. Zhang, B. Xu, S. Yue, H. Guo, Y. Luo, Alkali-treated graphene oxide as a solid base catalyst: Synthesis and electrochemical capacitance of graphene/carbon composite aerogels, *J. Mater. Chem.* 21 (2011) 18537–18539.
- [66] A. Sasidharan, L.S. Panchakarla, P. Chandran, D. Menon, S. Nair, C.N.R. Rao, M. Koyakutty, Differential nano-bio interactions and toxicity effects of pristine versus functionalized graphene, *Nanoscale* 3 (2011) 2461–2464.
- [67] L. Wang, Y. Tian, H. Ding, J. Li, Microstructure and properties of organosoluble polyimide/silica hybrid films, *Eur. Polym. J.* 42 (2006) 2921–2930.
- [68] R.K.Y. Fu, I.T.L. Cheung, Y.F. Mei, C.H. Shek, G.G. Siu, P.K. Chu, W.M. Yang, Y.X. Leng, Y.X. Huang, X.B. Tian, S.Q. Yang, Surface modification of polymeric materials by plasma immersion ion implantation, *Nucl. Instrum. Meth. B.* 237 (2005) 417–421.
- [69] L. Cui, Y. Liu, X. He, Iron(II) tetraaminophthalocyanine functionalized graphene: Synthesis, characterization and their application in direct methanol fuel cell, *J. Electroanal. Chem.* 727 (2014) 91–98.
- [70] F. Ma, J. Yao, Y. Zhang, Y. Wei, Oxygen vacancy promoting adsorption property of BiOI microspheres modified with SDS, *Chinese Chem. Lett.* 29 (2018) 1689–1691.
- [71] X. Qian, D. Yue, Z. Tian, M. Reng, Y. Zhu, M. Kan, T. Zhang, Y. Zhao, Carbon quantum dots decorated  $\text{Bi}_2\text{WO}_6$  nanocomposite with enhanced photocatalytic oxidation activity for VOCs, *Appl. Catal. B-Environ.* 193 (2016) 16–21.
- [72] F. Duan, Y. Zheng, M. Chen, Flowerlike  $\text{PtCl}_4/\text{Bi}_2\text{WO}_6$  composite photocatalyst with enhanced visible-light-induced photocatalytic activity, *Appl. Surf. Sci.* 257 (2011) 1972–1978.
- [73] L. Liu, H. Xu, H. Li, Y. Xu, J. Xia, S. Yin, Synthesis and characterization of the efficient visible-light-induced photocatalyst AgBr and its photodegradation activity, *J. Phys. Chem. Solids* 73 (2012) 523–529.
- [74] X.-X. Wei, H. Cui, S. Guo, L. Zhao, W. Li, Hybrid BiOBr- $\text{TiO}_2$  nanocomposites with high visible light photocatalytic activity for water treatment, *J. Hazard. Mater.* 263 (2013) 650–658.
- [75] Y. Li, Z. Wang, B. Huang, Y. Dai, X. Zhang, X. Qin, Synthesis of BiOBr-PVP hybrids with enhanced adsorption-photocatalytic properties, *Appl. Surf. Sci.* 347 (2015) 258–264.
- [76] J. Xiong, Y. Liu, C. Cao, L. Shen, W. Wu, S. Liang, R. Liang, L. Wu, An architecture of  $\text{CdS}/\text{H}_2\text{TiO}_5\text{O}_{11}$  ultrathin nanobelt for photocatalytic hydrogenation of 4-nitroaniline with highly efficient performance, *J. Mater. Chem. A* 3 (2015) 6935–6942.
- [77] W. Huang, N. Liu, X. Zhang, M. Wu, L. Tang, Metal organic framework g- $\text{C}_3\text{N}_4/\text{MIL}-53(\text{Fe})$  heterojunctions with enhanced photocatalytic activity for Cr(VI) reduction under visible light, *Appl. Surf. Sci.* 425 (2017) 107–116.
- [78] R. Liang, L. Shen, F. Jing, W. Wu, N. Qin, R. Lin, L. Wu,  $\text{NH}_2$ -mediated indium metal-organic framework as a novel visible-light-driven photocatalyst for reduction of the aqueous Cr(VI), *Appl. Catal. B-Environ.* 162 (2015) 245–251.
- [79] L. Shen, L. Huang, S. Liang, R. Liang, N. Qin, L. Wu, Electrostatically derived self-assembly of  $\text{NH}_2$ -mediated zirconium MOFs with graphene for photocatalytic reduction of Cr(VI), *RSC Adv.* 4 (2014) 2546–2549.
- [80] A.A. Oladipo, MIL-53 (Fe)-based photo-sensitive composite for degradation of organochlorinated herbicide and enhanced reduction of Cr(VI), *Process Saf. Environ.* 116 (2018) 413–423.
- [81] S. Luo, F. Qin, Y.A. Ming, H. Zhao, Y. Liu, R. Chen, Fabrication uniform hollow  $\text{Bi}_2\text{S}_3$  nanospheres via Kirkendall effect for photocatalytic reduction of Cr(VI) in electroplating industry wastewater, *J. Hazard. Mater.* 340 (2017) 253–262.
- [82] F. Xu, H. Chen, C. Xu, D. Wu, Z. Gao, Q. Zhang, K. Jiang, Ultra-thin  $\text{Bi}_2\text{WO}_6$  porous nanosheets with high lattice coherence for enhanced performance for photocatalytic reduction of Cr(VI), *J. Colloid Interf. Sci.* 525 (2018) 97–106.
- [83] H. Xu, Z. Wu, M. Ding, X. Gao, Microwave-assisted synthesis of flower-like BN/BiOCl composites for photocatalytic Cr(VI) reduction upon visible-light irradiation, *Mater. Design* 114 (2017) 129–138.
- [84] F. Hashemzadeh, A. Gaffarinejad, R. Rahimi, Porous p-NiO/n- $\text{Nb}_2\text{O}_5$  nanocomposites prepared by an EISA route with enhanced photocatalytic activity in simultaneous Cr(VI) reduction and methyl orange decolorization under visible light irradiation, *J. Hazard. Mater.* 286 (2015) 64–74.
- [85] Q. Yuan, L. Chen, M. Xiong, J. He, S.-L. Luo, C.-T. Au, S.-F. Yin,  $\text{Cu}_2\text{O}/\text{BiVO}_4$  heterostructures: Synthesis and application in simultaneous photocatalytic oxidation of organic dyes and reduction of Cr(VI) under visible light, *Chem. Eng. J.* 255 (2014) 394–402.
- [86] X. Hu, W. Wang, G. Xie, H. Wang, X. Tan, Q. Jin, D. Zhou, Y. Zhao, Ternary assembly of g- $\text{C}_3\text{N}_4$ /graphene oxide sheets/ $\text{BiFeO}_3$  heterojunction with enhanced photoreduction of Cr(VI) under visible-light irradiation, *Chemosphere* 216 (2019) 733–741.
- [87] N. Wang, L. Zhu, K. Deng, Y. She, Y. Yu, H. Tang, Visible light photocatalytic reduction of Cr(VI) on  $\text{TiO}_2$  in situ modified with small molecular weight organic acids, *Appl. Catal. B-Environ.* 95 (2010) 400–407.
- [88] J.K. Yang, S.M. Lee, M.S. Siboni, Effect of different types of organic compounds on the photocatalytic reduction of Cr(VI), *Environ. Technol.* 33 (2012) 2027–2032.
- [89] S. Weng, J. Hu, M. Lu, X. Ye, Z. Pei, M. Huang, L. Xie, S. Lin, P. Liu, In situ photogenerated defects on surface-complex BiOCl (010) with high visible-light photocatalytic activity: A probe to disclose the charge transfer in BiOCl (010)/surface-complex system, *Appl. Catal. B-Environ.* 163 (2015) 205–213.
- [90] Y. Wang, K. Hang, N.A. Anderson, T. Lian, Comparison of electron transfer dynamics in molecule-to-nanoparticle and intramolecular charge transfer complexes, *J. Phys. Chem. B.* 107 (2003) 9434–9440.
- [91] N. Wang, L. Zhu, Y. Huang, Y. She, Y. Yu, H. Tang, Drastically enhanced visible-light photocatalytic degradation of colorless aromatic pollutants over  $\text{TiO}_2$  via a charge-transfer-complex path: A correlation between chemical structure and degradation rate of the pollutants, *J. Catal.* 266 (2009) 199–206.
- [92] M.M. Joshi, N.K. Labhsetwar, P.A. Mangrulkar, S.N. Tijare, S.P. Kamble, S.S. Rayalu, Visible light induced photoreduction of methyl orange by N-doped mesoporous titania, *Appl. Catal. A-Gen.* 357 (2009) 26–33.
- [93] K. Vignesh, R. Priyanka, M. Rajarajan, A. Suganthi, Photoreduction of Cr(VI) in water using  $\text{Bi}_2\text{O}_3\text{-ZrO}_2$  nanocomposite under visible light irradiation, *Mater. Sci. Eng. B.* 178 (2013) 149–157.
- [94] C. Zhao, C.-C. Wang, J.-Q. Li, C.-Y. Wang, P. Wang, Z.-J. Pei, Dissolved organic matter in urban stormwater runoff at three typical regions in Beijing: chemical composition, structural characterization and source identification, *RSC Adv.* 5 (2015) 73490–73500.
- [95] C. Zhao, Z. Wang, C. Wang, X. Li, C.-C. Wang, Photocatalytic degradation of DOM in urban stormwater runoff with  $\text{TiO}_2$  nanoparticles under UV light irradiation: EEM-PARAFAC analysis and influence of co-existing inorganic ions, *Environ. Pollut.* 243 (2018) 177–188.
- [96] X. Zhao, P. Du, Z. Cai, T. Wang, J. Fu, W. Liu, Photocatalysis of bisphenol A by an easy-settling titania/titanate composite: Effects of water chemistry factors, degradation pathway and theoretical calculation, *Environ. Pollut.* 232 (2018) 580–590.
- [97] W.-W. Tang, G.-M. Zeng, J.-L. Gong, J. Liang, P. Xu, C. Zhang, B.-B. Huang, Impact of humic/fulvic acid on the removal of heavy metals from aqueous solutions using nanomaterials: a review, *Sci. Total Environ.* 468–469 (2014) 1014–1027.
- [98] C. Wang, L. Zhu, M. Wei, P. Chen, G. Shan, Photolytic reaction mechanism and impacts of coexisting substances on photodegradation of bisphenol A by  $\text{Bi}_2\text{WO}_6$  in water, *Water Res.* 46 (2012) 845–853.
- [99] B. Qiu, Y. Wang, D. Sun, Q. Wang, X. Zhang, B.L. Weeks, R. O'Connor, X. Huang, S. Wei, Z. Guo, Cr(VI) removal by magnetic carbon nanocomposites derived from cellulose at different carbonization temperatures, *J. Mater. Chem. A* 3 (2015) 9817–9825.
- [100] K. Li, Y. Liang, J. Yang, G. Yang, H. Zhang, K. Wang, R. Xu, X. Xie, Glucose-induced fabrication of Bi/ $\alpha\text{-Fe}_2\text{O}_3\cdot 2\text{H}_2\text{O}$  heterojunctions: a bifunctional catalyst with enhanced photocatalytic and Fenton oxidation efficiency, *Catal. Sci. Technol.* 9 (2019) 2543–2552.
- [101] S. Chen, Y. Hu, S. Meng, X. Fu, Study on the separation mechanisms of photo-generated electrons and holes for composite photocatalysts g- $\text{C}_3\text{N}_4\text{-WO}_3$ , *Appl. Catal. B-Environ.* 150–151 (2014) 564–573.
- [102] Q. Liu, C. Zeng, L. Ai, Z. Hao, J. Jiang, Boosting visible light photoreactivity of photoactive metal-organic framework: Designed plasmonic Z-scheme  $\text{Ag}/\text{AgCl}/\text{MIL}-53\text{-Fe}$ , *Appl. Catal. B-Environ.* 224 (2018) 38–45.
- [103] L. Ai, J. Su, M. Wang, J. Jiang, Bamboo-structured nitrogen-doped carbon nanotube coencapsulating cobalt and molybdenum carbide nanoparticles: An efficient bifunctional electrocatalyst for overall water splitting, *ACS Sustain. Chem. Eng.* 6 (2018) 9912–9920.
- [104] Y. Liu, C. Zeng, L. Ai, J. Jiang, Boosting charge transfer and hydrogen evolution performance of CdS nanocrystals hybridized with  $\text{MoS}_2$  nanosheets under visible light irradiation, *Appl. Surf. Sci.* 484 (2019) 692–700.
- [105] Z. Niu, C. Qiu, J. Jiang, L. Ai, Hierarchical Co-PeP branched heterostructures for highly efficient electrocatalytic water splitting, *ACS Sustain. Chem. Eng.* 7 (2019) 2335–2342.
- [106] C. Pan, J. Xu, Y. Wang, D. Li, Y. Zhu, Dramatic Activity of  $\text{C}_3\text{N}_4/\text{BiPO}_4$  Photocatalyst with core/shell structure formed by self-assembly, *Adv. Funct. Mater.* 22 (2012) 1518–1524.
- [107] Y. Hong, C. Li, B. Yin, D. Li, Z. Zhang, B. Mao, W. Fan, W. Gu, W. Shi, Promoting visible-light-induced photocatalytic degradation of tetracycline by an efficient and stable beta- $\text{Bi}_2\text{O}_3$ /g- $\text{C}_3\text{N}_4$  core/shell nanocomposite, *Chem. Eng. J.* 338 (2018) 137–146.
- [108] L.-P. Sun, S.-Y. Niu, J. Jin, G.-D. Yang, L. Ye, Crystal structure and surface photovoltage of a series of Ni(II) coordination supramolecular polymer, *Inorg. Chem. Commun.* 9 (2006) 679–682.
- [109] X. Jin, L. Ye, H. Wang, Y. Su, H. Xie, Z. Zhong, H. Zhang, Bismuth-rich strategy induced photocatalytic molecular oxygen activation properties of bismuth oxalogen: the case of  $\text{Bi}_{24}\text{O}_{31}\text{Cl}_{10}$ , *Appl. Catal. B-Environ.* 165 (2015) 668–675.
- [110] A.D. Bokare, W. Choi, Advanced oxidation process based on the Cr(III)/Cr(VI)

- redox cycle, *Environ. Sci. Technol.* 45 (2011) 9332–9338.
- [111] L. Wang, X. Li, W. Teng, Q. Zhao, Y. Shi, R. Yue, Y. Chen, Efficient photocatalytic reduction of aqueous Cr(VI) over flower-like  $\text{SnIn}_4\text{S}_8$  microspheres under visible light illumination, *J. Hazard. Mater.* 244–245 (2013) 681–688.
- [112] Y. Deng, L. Tang, G. Zeng, C. Feng, H. Dong, J. Wang, H. Feng, Y. Liu, Y. Zhou, Y. Pang, Plasmonic resonance excited dual Z-scheme  $\text{BiVO}_4/\text{Ag}/\text{Cu}_2\text{O}$  nanocomposite: synthesis and mechanism for enhanced photocatalytic performance in recalcitrant antibiotic degradation, *Environ. Sci-Nano* 4 (2017) 1494–1511.
- [113] J.-C. Wang, J. Ren, H.-C. Yao, L. Zhang, J.-S. Wang, S.-Q. Zang, L.-F. Han, Z.-J. Li, Synergistic photocatalysis of Cr(VI) reduction and 4-Chlorophenol degradation over hydroxylated  $\alpha\text{-Fe}_2\text{O}_3$  under visible light irradiation, *J. Hazard. Mater.* 311 (2016) 11–19.
- [114] B. Xu, H. Maimaiti, S. Wang, A. Awati, Y. Wang, J. Zhang, T. Chen, Preparation of coal-based graphene oxide/ $\text{SiO}_2$  nanosheet and loading ZnO nanorod for photocatalytic Fenton-like reaction, *Appl. Surf. Sci.* (2019), <https://doi.org/10.1016/j.apsusc.2019.143835>.
- [115] X.-H. Yi, S.-Q. Ma, X.-D. Du, C. Zhao, H. Fu, P. Wang, C.-C. Wang, The facile fabrication of 2D/3D Z-scheme  $\text{g-C}_3\text{N}_4/\text{UiO-66}$  heterojunction with enhanced photocatalytic Cr(VI) reduction performance under white light, *Chem. Eng. J.* 375 (2019) 121944–121957.
- [116] Y. Chen, L. Zhang, L. Ning, C. Zhang, H. Zhao, B. Liu, H. Yang, Superior photocatalytic activity of porous wurtzite ZnO nanosheets with exposed 001 facets and a charge separation model between polar (001) and (001 $\bar{}$ ) surfaces, *Chem. Eng. J.* 264 (2015) 557–564.